Energy Control of Modular Multilevel Converters for Drive Applications at Low Frequency Using General Averaging

Qiuye Gui, Hendrik Fehr, and Albrecht Gensior

***Abstract*—This article focuses on the energy control of modular multilevel converters (MMCs) for drive applications at low frequency. Utilizing the general averaging method, this work extends the results for MMC dc-operation in a previous work to low-frequency operation, and inherits all improvements with respect to model based controller design in dc-operation analysis, compared to other state-of-art approaches. The proposed energy control system—with either a constant or a stationary regime as reference for the instantaneous MMC energies—is proven to be globally stable, where the stability of the constant reference in low-frequency operation is confirmed theoretically, which is missing in state-of-art research. Besides, an optimization cooperating with two common-mode voltages for the energy control and compensation of ripples at low frequency is provided. The experiments verify the stability of the energy control system, and provide comparison between the two energy references in low-frequency operation for the first time, confirming the constant energy reference as a noteworthy option. The optimization improves the MMC performance, including the stationary operation generated by the optimization in cooperation with the approximated trapezoidal common-mode voltage as an improvement of a state-of-art solution in the sense of smaller arm currents RMS and cell capacitor voltage fluctuation.**

***Index Terms*—Control theory, modular multilevel converters (MMC), motor drives, optimization, stability.**

I. Introduction

COMPARED with conventional two-level voltage-source converters, the modular multilevel converter (MMC) topology shows superior characteristics w.r.t. distortion in the ac-side voltages and currents, industrial scalability, operational power loss, and electromagnetic compatibility [1]. As a result, researches have been reported focusing on, e.g. HVDC-transmission [2], [3], [4] and drive applications [5], [6], [7], [8], [9]. This work focuses on the energy control issue of MMCs with half-bridge cells in low-frequency mode (lf-mode), i.e., an ac machine is fed at low stator electrical frequency (including 0 Hz case as in dc operation [10]), see Fig. 1.

Manuscript received 13 July 2023; revised 3 November 2023 and 12 January 2024; accepted 20 January 2024. Date of publication 30 January 2024; date of current version 20 March 2024. This work was supported by Deutsche Forschungsgemeinschaft, DFG under Grant GE 2502/5-1. Recommended for publication by Associate Editor Makoto Hagiwara. *(Corresponding author: Qiuye Gui.)*

The authors are with the Power Electronics and Control Group, Technische Universiät Ilmenau, 98693 Ilmenau, Germany (e-mail: qiuye.gui@tu-ilmenau.de; hendrik.fehr@tu-ilmenau.de; albrecht.gensior@tu-ilmenau.de).

Color versions of one or more figures in this article are available at https://doi.org/10.1109/TPEL.2024.3360000.

Digital Object Identifier 10.1109/TPEL.2024.3360000

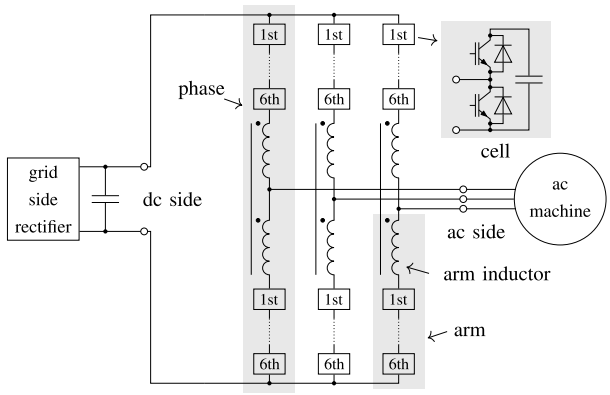

Fig. 1. Scheme of the application.

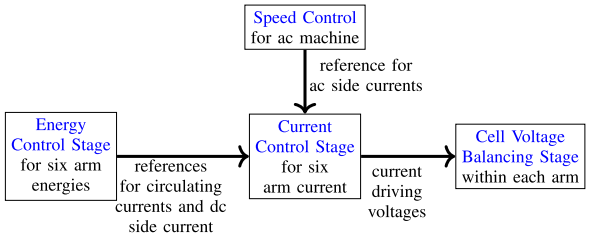

Fig. 2. Structure of the control for an MMC for drive applications.

As discussed in [11], a commonly employed MMC control structure is shown in Fig. 2. The task of the innermost stage is the cell-voltage balancing within each arm which can be solved by a sorting algorithm implemented in the modulation. It usually requires the current-driving voltages from the outer stage for current control, the common-mode voltage, the direction of the arm currents, and the value of each cell capacitor voltage. Works contributing to this task can be found in [12], [13], and [14]. As presented in [5], [7], [15], and [16], the task in the current control stage is usually split into the control of the common-mode components, i.e., the dc-side current and the circulating currents, and the differential-mode components, i.e., the ac-side currents. For drive applications, the reference for the ac-side currents is generated by the speed control of the ac machine, while the references for the common-mode components are provided by the outermost energy-control stage.

This work focuses on the outermost stage, where algorithms are employed to retain the stored energy in each arm. The energy

control is challenging due to the strong coupling [17], [18], the underactuation of the energy model [19], [20], and the lack of meaningful stationary operating points in which all arm energies remain constant [8], [21], [22]. State-of-art approaches for this stage include the average value control in [5], [9], [23], and [24], the dynamic phasor model [25], [26], and the harmonic state-space approach [27], [28]. Although widely accepted, they suffer from some drawbacks or open issues. The average control lacks a model for the average energy with mathematical background and cannot confirm stability w.r.t. the energy ripples. The other two approaches consider the dynamics of all energy harmonics, but increase the system order substantially which increases the control design effort. The works in [10] and [19] overcome the drawbacks mentioned above. In contrast to [19] which derives an average energy model limited to a finite time interval, a simple systematic controller design framework for (nonlinear) time-periodic systems was presented in [10]. The framework relies on a theorem in [29] using an averaging method, and thus extends the stability analysis in [19] to the whole time range $t \in [0, \infty)$. Furthermore, the method in [10] confirmed the energy control system to be globally stable. This is an improvement over the results in [7], [27], and [30], since the analyses there are only concerned to the region of attraction in an uncertain small neighborhood of a stationary operating regime/point.

A. From DC-Operation (0 Hz) to Low-Frequency Mode

With the advantages/improvements of [10] mentioned above, it is reasonable and beneficial to extend the results in [10] for MMC dc-operation (feeding a machine with zero stator electrical frequency) to lf-mode in this text. Although the controller design framework in [10] was compatible with time-periodic systems and accomplishes the energy control design of an MMC in dc-operation, it is not compatible with the lf-mode. As reported in [5], [7], [31], and [32], in order to avoid energy ripples at low frequency with undesired large amplitude, predetermined high-frequency components are injected to the arm currents and common-mode voltage in order to compensate the low-frequency power or energy ripples. As a result, the MMC arm energies are influenced by two different frequencies: The stator electrical frequency ω_{m} and the injected predetermined high frequency ω_{cm}. In this case, the system is considered as time-almost-periodic. Although several equivalent definitions for time-almost-periodic functions were given in [33], in this text, we focus on the ones which are the sum of several time-periodic functions with individual frequencies [29]. Generally speaking, no period as defined for time-periodic systems can be found for time-almost-periodic systems. This means that the averaging method in the framework in [10] cannot accomplish the controller design in lf-mode. To this phenomenon, a more detailed illustration with the MMC model will be given in Section IV. Fortunately, the general averaging provided by [29, Theorem 10.5] extends the averaging method used in [10] to more general cases and is compatible with almost-periodic cases. Thus, the general averaging method will be utilized to accomplish the energy control task in lf-mode.

B. Contributions and Outline

In this context, the present work contributes as follows.

1) Based on [29, Theorem 10.5], this work utilizes the general averaging method for the energy control task of an MMC for drive application at low frequency (lf-mode). This method extends the averaging method for dc-operation (0 Hz) in [10] to the almost-periodic cases in lf-mode. Thus, this work covers the results for dc-operation (0 Hz) in [10] as a specific case, and inherits all improvements of [10] compared to [5], [9], [19], [23], [24], [25], [26], [27], and [28] (as mentioned before in Section I-A).
2) The analysis leads to the proposed control system for the MMC energies in lf-mode. As an extension from the stability analysis for dc-operation in [10], this work provides a rigorous global stability analysis of the energy control system for lf-mode, in which either a stationary operating regime (as in [5]) or a constant (as in [17] and [34]) can be chosen as the reference for the instantaneous MMC energies. Analogous to [10], the analysis offers a global stability, unlike [7], [27], and [30] which use linearization, and thus can only provide a region of attraction in an uncertain small neighborhood of a stationary operating regime/point. The validity of a constant reference for the instantaneous MMC energies in lf-mode is provided by dedicated theoretical analysis for the first time.
3) For the energy controller and compensation of ripples at low frequency, besides a simple choice (similar to [5]), an optimization is derived which enables all feasible current harmonics for the control and compensation task. It cooperates with two common-mode voltages: The one in [6, Sec. IV-B] and an approximated trapezoidal waveform.
4) The experiments verify the stability of the energy control system, including the theoretical conclusions. The results provide a comparison between the constant energy reference [17], [34] and the regime as reference [5] for the first time, and confirms the constant reference as a noteworthy option. The optimization improves the MMC performance, including the optimized stationary regime/operation generated by the optimization in cooperation with v_{y0}^{trpz} as an improvement of [7, Strategy II] in the sense of smaller arm current Root Mean Square (RMS) and cell capacitor voltage fluctuation.

The rest of this article is organized as follows. The theoretical results w.r.t. general averaging method in [29] and the idea of control design are illustrated briefly in Section II. According to the energy model given in Section III and following the idea in Section II, the design of energy control and compensation of ripples at low frequency are presented in Section IV. The experimental results are discussed in Section V. Finally, Section VI concludes this article.

II. General Averaging Method

To make the analysis in Section IV more understandable, it is beneficial to introduce general averaging method in [29], and the main idea of the proposed controller design briefly.

A. General Averaging and Associated Results from [29]

The averaging method [29]

$$\overline{\boldsymbol{f}}(\boldsymbol{x}) = \frac{1}{T}\int_0^T \boldsymbol{f}(t,\boldsymbol{x})\,\mathrm{d}t, \quad \text{for } 0 < T < \infty \tag{1}$$

used in the framework in [10] is compatible with the time-periodic function $\boldsymbol{f}$, given by

$$\boldsymbol{f}(t,\boldsymbol{x}) = \boldsymbol{f}(t+T,\boldsymbol{x}). \tag{2}$$

Notice that the state vector $\boldsymbol{x}$ is regarded as time-independent while considering (1) and (2). However, for the almost periodic function which is the sum of several time-periodic functions with individual frequencies, i.e.,

$$\boldsymbol{f}(t,\boldsymbol{x}) = \sum_{n=1}^{N} \boldsymbol{f}_n(t,\boldsymbol{x}) \tag{3a}$$

$$\boldsymbol{f}_n(t,\boldsymbol{x}) = \boldsymbol{f}_n(t+T_n,\boldsymbol{x}) \tag{3b}$$

$$T_{n_1} \neq T_{n_2} \quad \text{for } n_1 \neq n_2 \tag{3c}$$

the averaging method (1) is no longer compatible. This is because in this case one cannot find any period $T > 0$ for all $\boldsymbol{f}_n$, once the ratio T_{n_1}/T_{n_2} of two individual periods is irrational. Instead, the general averaging [29] extends the averaging method (1) by

$$\overline{\boldsymbol{f}}(\boldsymbol{x}) = \lim_{T\to\infty}\frac{1}{T}\int_0^T \boldsymbol{f}(t,\boldsymbol{x})\,\mathrm{d}t. \tag{4}$$

Same as in (1) and (2), the state vector $\boldsymbol{x}$ is regarded as time-independent while considering (4). Confirmed by [29], for almost periodic functions (3), the general average is the sum of the average of its components $\boldsymbol{f}_n$ in the sense of (1).

Associated with the general averaging (4), the main results of [29, Theorem 10.5] can be summarized briefly as follows: Under some conditions, for a sufficiently small perturbation parameter ε, the solution $\boldsymbol{x}(t)$ of the original system

$$\dot{\boldsymbol{x}} = \varepsilon \boldsymbol{f}(t,\boldsymbol{x},\varepsilon) \tag{5}$$

lies in a small neighborhood of the solution $\overline{\boldsymbol{x}}(t)$ of the average system

$$\dot{\overline{\boldsymbol{x}}} = \varepsilon \overline{\boldsymbol{f}}(\overline{\boldsymbol{x}}) \tag{6}$$

for $\forall t \in [0,\infty)$, and the origin $\boldsymbol{x} = \boldsymbol{0}$ of the original system (5) is exponentially stable if it is an equilibrium point, i.e.,

$$\boldsymbol{f}(t,\boldsymbol{0},\varepsilon) = \boldsymbol{0}. \tag{7}$$

Here, the state of the average system (6) is represented by $\overline{\boldsymbol{x}}$ rather than $\boldsymbol{x}$ in order to distinguish from the original system (5). One may refer to Definition 1 and Theorem 1 in Appendix for the detailed mathematical version.

B. Idea of Control Design

One may consider the original system (5) as the dynamics of a closed-loop system with $\boldsymbol{x}$ as the control error. In this context, this theorem provides an alternative method for the controller design of a closed-loop system, i.e., instead of designing a controller directly at the complicated time-varying original system (5), a controller for the original system (5) can be designed at the simplified time-invariant average system (6) derived by (4). Moreover, the remaining error of (5) vanishes once the additional condition (7) is also fulfilled.

Based on the modeling in Section III, the design of energy control and compensation of ripples at low frequency in MMC lf-mode follows the aforementioned idea, as will be presented in Section IV.

III. Energy Model

For the energy control task in this work, the energy model

$$\dot{e}_{s0} = v_{\mathrm{DC}} i_{s0} - \mathrm{Re}\left(\underline{v}_y^* \underline{i}\right) \tag{8a}$$

$$\dot{e}_{d0} = -2v_{y0} i_{s0} - \mathrm{Re}\left(\underline{i}_s^* \underline{v}_y\right) \tag{8b}$$

$$\dot{\underline{e}}_s = v_{\mathrm{DC}} \underline{i}_s - \underline{v}_y^* \underline{i}^* - 2\underline{i} v_{y0} \tag{8c}$$

$$\dot{\underline{e}}_d = v_{\mathrm{DC}} \underline{i} - \underline{i}_s^* \underline{v}_y^* - 2\underline{i}_s v_{y0} - 2i_{s0}\underline{v}_y \tag{8d}$$

from [10], [19] is considered. The transformed energies can be summarized as $\boldsymbol{e} = (e_{s0}\ e_{d0}\ \mathrm{Re}(\underline{e}_s)\ \mathrm{Im}(\underline{e}_s)\ \mathrm{Re}(\underline{e}_d)\ \mathrm{Im}(\underline{e}_d))^{\mathrm{T}}$, where e_{s0} denotes the scaled total stored energy, e_{d0} denotes the scaled total vertical energy difference, while $\underline{e}_s$ and $\underline{e}_d$ denote the complex energy sum and difference, respectively. The currents i_{s0}, $\underline{i}_s$, and $\underline{i}$ denote the scaled dc current, the circulating current, and the complex ac-side current, respectively. The variables v_{DC}, v_{y0}, and $\underline{v}_y$ denote the dc link voltage, the common-mode voltage, and the complex ac-side voltage, respectively. Details of the variable definition and transformation can be found in [19] and [35]. Here, the current dynamics are neglected since they are considered to be "much faster" than the energy dynamics, i.e., the current control error is assumed to be zero in the context of this article. In contrast, the dynamics of the mechanical subsystem of the motor is generally considered to be "much slower" such that the stator electrical frequency ω_{m} is assumed to be independent of time as far as the energy control is concerned. Hence, only the fundamental component with constant amplitude and angle is considered for the ac side current $\underline{i}$ and voltage $\underline{v}_y$. Similar as in [5], [7], [31], and [32], in order to accomplish the energy control task and compensate undesired energy or power ripples at low frequency, harmonics w.r.t. a high predetermined frequency $\omega_{\mathrm{cm}} \gg |\omega_{\mathrm{m}}|$ are injected in $\underline{i}_s$, i_{s0}, and v_{y0}. To sum up, the current and voltage injection to the energy model (8) is given by (9) shown at the bottom of next page, with $|n_1\omega_{\mathrm{m}}| < \omega_{\mathrm{cm}}$ where the coefficients $\underline{I}^{[1,0]}$, $\underline{V}_y^{[1,0]}$, $\underline{V}_{y0}^{[0,n]}$, and $V_{\mathrm{DC}}^{[0,0]}$ are constant, and the condition $|n_1\omega_{\mathrm{m}}| < \omega_{\mathrm{cm}}$ ensures that the current harmonics $\underline{I}_{s0}^{[n_1,n_2]}(\cdot,\cdot)\mathrm{e}^{j(n_1\omega_{\mathrm{m}}+n_2\omega_{\mathrm{cm}})t}$ and $\underline{I}_s^{[n_1,n_2]}(\cdot,\cdot)\mathrm{e}^{j(n_1\omega_{\mathrm{m}}+n_2\omega_{\mathrm{cm}})t}$ will not convert to a component without explicit dependency on t. The stator electrical frequency satisfies $|\omega_{\mathrm{m}}| \geq 0$, where $\omega_{\mathrm{m}} = 0$ coincides with the dc-operation studied in [10]. The coefficients of i_{s0} and $\underline{i}_s$ might depend on the energy error $\boldsymbol{e}_{\mathrm{err}} = \boldsymbol{e} - \boldsymbol{e}_{\mathrm{ref}}$ and its integral $\boldsymbol{e}_{\mathrm{err,I}}$, obtained from $\dot{\boldsymbol{e}}_{\mathrm{err,I}} = \boldsymbol{e}_{\mathrm{err}}$, to facilitate the control task. This covers the case in which the current coefficients are not constant due to the controller behavior.

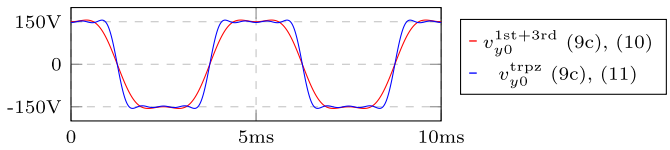

Fig. 3. Common-mode voltages: 1st+3 rd harmonics $v_{y0}^{1\text{st}+3\,\text{rd}}$ and approximated trapezoidal waveform v_{y0}^{trpz}.

A. Common-Mode Voltage

In (9c), the coefficient $\underline{V}_{y0}^{[0,n]}$ is assumed to be independent of the error state. Despite this, the following analysis in Section IV is also compatible with error dependent $\underline{V}_{y0}^{[0,n]}(\boldsymbol{e}_{\text{err}}, \boldsymbol{e}_{\text{err,I}})$ as feasible controller output, as will be mentioned in Section IV-B. Similar as in [10], two different common-mode voltage injections, shown in Fig. 3, are considered

1) The choice (9c) with

$$n \in \mathbb{N}_{\text{cm}} = \{1, 3\}\,, \quad \underline{V}_{y0}^{[0,1]} = 0.15 \cdot V_{\text{DC}}^{[0,0]} \tag{10a}$$

$$\underline{V}_{y0}^{[0,3]} = -\left|\underline{V}_{y0}^{[0,1]}\right| / 6 \cdot \mathrm{e}^{j3\arg\left(\underline{V}_{y0}^{[0,1]}\right)} \tag{10b}$$

drawn in red. Equivalent choice can be found in [6, Sec. IV-B]. Due to the low electromotive force (EMF) in the low frequency operation, the required cell terminal voltage is dominated by the common-mode voltage. Thus, compared with the sinusoidal waveform in [5], [31], [36], [6, Sec. IV-A], this variant exploits the third harmonic in order to allow for an increased first harmonic $\underline{V}_{y0}^{[0,1]}$ and avoids saturation, as pointed out in [6].

2) Alternatively, choosing (9c) with

$$n \in \mathbb{N}_{\text{cm}} = \{1, 3, 5, 7\} \tag{11a}$$

$$\underline{V}_{y0}^{[0,n]} = \frac{V_{\text{DC}}^{[0,0]}}{4} \frac{\sin\left(n\frac{\pi}{2}\right)}{n\frac{\pi}{2}} \frac{\sin\left(n\frac{\pi}{10}\right)}{n\frac{\pi}{10}} \tag{11b}$$

uses harmonics up to the 7th to approximate a trapezoidal waveform. This is shown in blue. This waveform with limited derivatives avoids sharp edges in the square waveform used in [6, Sec. IV-C], [7], [9], [37], [38], [39], [40], [41], which helps to avoid harmful motor bearing failures [31]. The approximated flat top allows the waveform to contain harmonics of high order with limited amplitude to avoid saturation. Similar choices include the exact trapezoidal waveform used in [34] and [42] and the smooth trigonometric function in [43] with the same maximal slope and peak voltage level as an exact trapezoidal waveform. As will be shown in (30) in Section IV-B, the finite harmonic order in (11) will also limit the current harmonic orders while using the proposed optimization, which is expected to have a better current control accuracy [6], [7], [37], compared with the exact trapezoidal waveform in [34] and [42] and the square waveform with infinite harmonic orders.

The same common-mode voltages are also used in [10] for dc-operation ($\omega_{\text{m}} = 0$) of MMC.

B. Reference for the Instantaneous MMC Energies

For the energy reference, defined by $\dot{\boldsymbol{e}}_{\text{ref}} := \boldsymbol{p}_{\text{ref}}(\omega_{\text{m}}t, \omega_{\text{cm}}t)$, two options apply as follows.

1) The first one is a stationary operating regime $\boldsymbol{e}_{\text{ref}} = \boldsymbol{e}_{\text{rgm}}$ alternating around a constant $\boldsymbol{E}$, where $\boldsymbol{p}_{\text{ref}}$ is almost periodic without any drift. Same idea can be found in [5]. The design of the regimes will be discussed in Section IV-D. The remaining control errors are desired to be zero, since the regimes fulfill the MMC energy model (8).
2) The second one is the constant $\boldsymbol{e}_{\text{ref}} = \boldsymbol{E}$ with $\boldsymbol{p}_{\text{ref}} = \boldsymbol{0}$. Same choice can be found in [17] and [34]. Remaining control errors are expected, since no meaningful stationary operating point of MMC energy exist. In other words, the resulting stationary energy ripples are expected to be only caused by the remaining errors. The stability of this option—which is missing in the state-of-art research for lf-mode—deserves a dedicated theoretical analysis, as will be provided in Section IV-E.

Same idea for energy reference can be found in [10] for dc-operation ($\omega_{\text{m}} = 0$) of MMC.

IV. Controller Design and Compensation of Ripples at Low Frequency

The design of energy controller and the compensation of ripples at low frequency in this section are based on the idea in Section II-B. In Section IV-A, by means of general averaging (4), the analysis is carried out to derive the average system for the

$$i_{s0} = I_{s0}^{[0,0]}\left(\boldsymbol{e}_{\text{err}}, \boldsymbol{e}_{\text{err,I}}\right) + \sum_{n\in\mathbb{Z}^+}\left(\underline{I}_{s0}^{[0,n]}\left(\boldsymbol{e}_{\text{err}}, \boldsymbol{e}_{\text{err,I}}\right)\mathrm{e}^{jn\omega_{\text{cm}}t} + \underline{I}_{s0}^{[0,n]*}\left(\boldsymbol{e}_{\text{err}}, \boldsymbol{e}_{\text{err,I}}\right)\mathrm{e}^{-jn\omega_{\text{cm}}t}\right)$$
$$+ \sum_{n_1\in\mathbb{Z}^+, n_2\in\mathbb{Z}}\left(\underline{I}_{s0}^{[n_1,n_2]}\left(\boldsymbol{e}_{\text{err}}, \boldsymbol{e}_{\text{err,I}}\right)\mathrm{e}^{j(n_1\omega_{\text{m}}+n_2\omega_{\text{cm}})t} + \underline{I}_{s0}^{[n_1,n_2]*}\left(\boldsymbol{e}_{\text{err}}, \boldsymbol{e}_{\text{err,I}}\right)\mathrm{e}^{-j(n_1\omega_{\text{m}}+n_2\omega_{\text{cm}})t}\right) \tag{9a}$$

$$\underline{i}_s = \sum_{n_1\in\mathbb{Z}, n_2\in\mathbb{Z}} \underline{I}_s^{[n_1,n_2]}\left(\boldsymbol{e}_{\text{err}}, \boldsymbol{e}_{\text{err,I}}\right)\mathrm{e}^{j(n_1\omega_{\text{m}}+n_2\omega_{\text{cm}})t} \tag{9b}$$

$$v_{y0} = \sum_{n\in\mathbb{N}_{\text{cm}}}\left(\underline{V}_{y0}^{[0,n]}\mathrm{e}^{jn\omega_{\text{cm}}t} + \underline{V}_{y0}^{[0,n]*}\mathrm{e}^{-jn\omega_{\text{cm}}t}\right), \quad \mathbb{N}_{\text{cm}}: \text{made up of all harmonic orders of } v_{y0} \tag{9c}$$

$$\underline{v}_y = \underline{V}_y^{[1,0]}\mathrm{e}^{j\omega_{\text{m}}t}, \quad \underline{i} = \underline{I}^{[1,0]}\mathrm{e}^{j\omega_{\text{m}}t}, \quad v_{\text{DC}} = V_{\text{DC}}^{[0,0]} \tag{9d}$$

controller design and the condition for compensation of ripples at low frequency. After finding the candidates in Section IV-B, the energy control system is obtained in Section IV-C, with the design of stationary operating regime given in Section IV-D. The stability of the energy control system is provided in Section IV-E.

A. Derivation of Average System and Condition for Compensation of Ripples at Low Frequency

Substituting the error definition $\boldsymbol{e}_{\text{err}} = \boldsymbol{e} - \boldsymbol{e}_{\text{ref}}$, the injection (9), and the definition $\dot{\boldsymbol{e}}_{\text{ref}} := \boldsymbol{p}_{\text{ref}}(\omega_{\text{m}}t, \omega_{\text{cm}}t)$ into the energy model (8) leads to the system

$$\begin{aligned}\dot{\boldsymbol{e}}_{\text{err}} = {} & \boldsymbol{p}_{\text{dc}}\left(\boldsymbol{e}_{\text{err}}, \boldsymbol{e}_{\text{err,I}}\right) + \boldsymbol{p}_{\text{lf}}\left(\omega_{\text{m}}t, \boldsymbol{e}_{\text{err}}, \boldsymbol{e}_{\text{err,I}}\right) \\ & + \boldsymbol{p}_{\text{hf}}\left(\omega_{\text{m}}t, \omega_{\text{cm}}t, \boldsymbol{e}_{\text{err}}, \boldsymbol{e}_{\text{err,I}}\right) \\ & - \boldsymbol{p}_{\text{ref}}\left(\omega_{\text{m}}t, \omega_{\text{cm}}t\right) \qquad (12a)\end{aligned}$$

$$\dot{\boldsymbol{e}}_{\text{err,I}} = \boldsymbol{e}_{\text{err}} \qquad (12b)$$

with (13) shown at the bottom of this page, and $|n_1\omega_{\text{m}}| < \omega_{\text{cm}}$ where $\boldsymbol{p}_{\text{dc}}$ denotes the power terms without explicit dependency on t, the term $\boldsymbol{p}_{\text{lf}}$ denotes the alternating powers at low frequency which is independent of the predetermined frequency ω_{cm} but with explicit dependency on $\omega_{\text{m}}t$, the remaining alternating power terms with explicit dependency on both, $\omega_{\text{m}}t$ and $\omega_{\text{cm}}t$, are represented by $\boldsymbol{p}_{\text{hf}}$ which is omitted for brevity. Finally, $(\boldsymbol{e}_{\text{err}}^{\text{T}} \quad \boldsymbol{e}_{\text{err,I}}^{\text{T}})^{\text{T}}$ represents the state variable.

The system (12) represents the dynamics of the energy error $(\boldsymbol{e}_{\text{err}}^{\text{T}} \quad \boldsymbol{e}_{\text{err,I}}^{\text{T}})^{\text{T}}$. However, it is still not in the form of (5), since the perturbation parameter is not defined yet. To achieve the form of (5), using the same choice in [10], the perturbation parameter can be chosen as $\varepsilon = 1/\omega_{\text{cm}}$, which means that ε can be reduced by increasing the predetermined frequency ω_{cm}. The change of time variable $\tau = \omega_{\text{cm}}t$ transforms (12) into

$$\begin{aligned}\frac{\text{d}}{\text{d}\tau}\boldsymbol{e}_{\text{err}} = {} & \varepsilon\left[\boldsymbol{p}_{\text{dc}}\left(\boldsymbol{e}_{\text{err}}, \boldsymbol{e}_{\text{err,I}}\right) + \boldsymbol{p}_{\text{lf}}\left(r\tau, \boldsymbol{e}_{\text{err}}, \boldsymbol{e}_{\text{err,I}}\right)\right] \\ & + \varepsilon\left[\boldsymbol{p}_{\text{hf}}\left(r\tau, \tau, \boldsymbol{e}_{\text{err}}, \boldsymbol{e}_{\text{err,I}}\right) - \boldsymbol{p}_{\text{ref}}\left(r\tau, \tau\right)\right] \qquad (14a)\end{aligned}$$

$$\frac{\text{d}}{\text{d}\tau}\boldsymbol{e}_{\text{err,I}} = \varepsilon\boldsymbol{e}_{\text{err}} \qquad (14b)$$

which is in the same form as (5) by regarding τ as the time variable. Here, the two frequencies are given by the relation $\omega_{\text{m}} = r\omega_{\text{cm}}$ and therefore $0 \leq |r| \ll 1$. By means of the ratio r, we can discuss the properties of the right-hand side of (14a)

$$\boldsymbol{p}_{\text{dc}}(\cdot,\cdot) = \left(p_{\text{dc,es0}} \quad p_{\text{dc,ed0}} \quad \text{Re}\left(\underline{p}_{\text{dc,es}}\right) \quad \text{Im}\left(\underline{p}_{\text{dc,es}}\right) \quad \text{Re}\left(\underline{p}_{\text{dc,ed}}\right) \quad \text{Im}\left(\underline{p}_{\text{dc,ed}}\right)\right)^{\text{T}} \qquad (13a)$$

$$\boldsymbol{p}_{\text{lf}}(\cdot,\cdot,\cdot) = \left(p_{\text{lf,es0}} \quad p_{\text{lf,ed0}} \quad \text{Re}\left(\underline{p}_{\text{lf,es}}\right) \quad \text{Im}\left(\underline{p}_{\text{lf,es}}\right) \quad \text{Re}\left(\underline{p}_{\text{lf,ed}}\right) \quad \text{Im}\left(\underline{p}_{\text{lf,ed}}\right)\right)^{\text{T}} \qquad (13b)$$

$$p_{\text{dc,es0}} = V_{\text{DC}}^{[0,0]} I_{s0}^{[0,0]}(\cdot,\cdot) - \text{Re}\left(\underline{V}_{y}^{[1,0]*}\underline{I}^{[1,0]}\right), \quad \underline{p}_{\text{dc,es}} = V_{\text{DC}}^{[0,0]}\underline{I}_{s}^{[0,0]}(\cdot,\cdot) \qquad (13c)$$

$$p_{\text{dc,ed0}} = -2\sum_{n\in\mathbb{N}_{\text{cm}}}\left(\underline{I}_{s0}^{[0,n]}(\cdot,\cdot)\,\underline{V}_{y0}^{[0,n]*} + \underline{I}_{s0}^{[0,n]*}(\cdot,\cdot)\,\underline{V}_{y0}^{[0,n]}\right) - \text{Re}\left(\underline{V}_{y}^{[1,0]*}\underline{I}_{s}^{[1,0]}(\cdot,\cdot)\right) \qquad (13d)$$

$$\underline{p}_{\text{dc,ed}} = -\underline{I}_{s}^{[-1,0]*}(\cdot,\cdot)\,\underline{V}_{y}^{[1,0]*} - 2\underline{I}_{s0}^{[1,0]*}(\cdot,\cdot)\,\underline{V}_{y}^{[1,0]} - 2\sum_{n\in\mathbb{N}_{\text{cm}}}\left(\underline{I}_{s}^{[0,-n]}(\cdot,\cdot)\,\underline{V}_{y0}^{[0,n]} + \underline{I}_{s}^{[0,n]}(\cdot,\cdot)\,\underline{V}_{y0}^{[0,n]*}\right) \qquad (13e)$$

$$p_{\text{lf,es0}} = \sum_{n_1\in\mathbb{Z}^+} V_{\text{DC}}^{[0,0]}\left(\underline{I}_{s0}^{[n_1,0]}(\cdot,\cdot)\,\text{e}^{jn_1\omega_{\text{m}}t} + \underline{I}_{s0}^{[n_1,0]*}(\cdot,\cdot)\,\text{e}^{-jn_1\omega_{\text{m}}t}\right) \qquad (13f)$$

$$\begin{aligned}p_{\text{lf,ed0}} = {} & -2\sum_{n_2\in\mathbb{N}_{\text{cm}},n_1\in\mathbb{Z}^+}\left(\underline{V}_{y0}^{[0,n_2]}\underline{I}_{s0}^{[n_1,n_2]*}(\cdot,\cdot) + \underline{V}_{y0}^{[0,n_2]*}\underline{I}_{s0}^{[n_1,-n_2]*}(\cdot,\cdot)\right)\text{e}^{-jn_1\omega_{\text{m}}t} \\ & -2\sum_{n_2\in\mathbb{N}_{\text{cm}},n_1\in\mathbb{Z}^+}\left(\underline{V}_{y0}^{[0,n_2]}\underline{I}_{s0}^{[n_1,-n_2]}(\cdot,\cdot) + \underline{V}_{y0}^{[0,n_2]*}\underline{I}_{s0}^{[n_1,n_2]}(\cdot,\cdot)\right)\text{e}^{jn_1\omega_{\text{m}}t} \\ & -\text{Re}\left(\sum_{n_1\in\mathbb{Z}\setminus\{1\}}\underline{V}_{y}^{[1,0]*}\underline{I}_{s}^{[n_1,0]}(\cdot,\cdot)\,\text{e}^{j(n_1-1)\omega_{\text{m}}t}\right) \qquad (13g)\end{aligned}$$

$$\underline{p}_{\text{lf,es}} = V_{\text{DC}}^{[0,0]}\sum_{n_1\in\mathbb{Z}\setminus\{0\}}\underline{I}_{s}^{[n_1,0]}(\cdot,\cdot)\,\text{e}^{jn_1\omega_{\text{m}}t} - \underline{V}_{y}^{[1,0]*}\underline{I}^{[1,0]*}\text{e}^{-j2\omega_{\text{m}}t} \qquad (13h)$$

$$\begin{aligned}\underline{p}_{\text{lf,ed}} = {} & V_{\text{DC}}^{[0,0]}\underline{I}^{[1,0]}\text{e}^{j\omega_{\text{m}}t} - \underline{V}_{y}^{[1,0]*}\sum_{n_1\in\mathbb{Z}\setminus\{-1\}}\underline{I}_{s}^{[n_1,0]*}(\cdot,\cdot)\,\text{e}^{-j(n_1+1)\omega_{\text{m}}t} - 2\underline{V}_{y}^{[1,0]}I_{s0}^{[0,0]}(\cdot,\cdot)\,\text{e}^{j\omega_{\text{m}}t} \\ & -2\sum_{n_1\in\mathbb{Z}\setminus\{0\},n_2\in\mathbb{N}_{\text{cm}}}\left(\underline{V}_{y0}^{[0,n_2]}\underline{I}_{s}^{[n_1,-n_2]}(\cdot,\cdot) + \underline{V}_{y0}^{[0,n_2]*}\underline{I}_{s}^{[n_1,n_2]}(\cdot,\cdot)\right)\text{e}^{jn_1\omega_{\text{m}}t} \\ & -2\underline{V}_{y}^{[1,0]}\sum_{n_1\in\mathbb{Z}^+}\underline{I}_{s0}^{[n_1,0]}(\cdot,\cdot)\,\text{e}^{j(n_1+1)\omega_{\text{m}}t} - 2\underline{V}_{y}^{[1,0]}\sum_{n_1\in\mathbb{Z}^+\setminus\{1\}}\underline{I}_{s0}^{[n_1,0]*}(\cdot,\cdot)\,\text{e}^{j(-n_1+1)\omega_{\text{m}}t} \qquad (13i)\end{aligned}$$

shortly, which also justify the necessity of using general averaging as follows.

1) Although the function $\boldsymbol{p}_{\text{lf}}(r\tau, \boldsymbol{e}_{\text{err}}, \boldsymbol{e}_{\text{err,I}})$ is periodic in τ for $|r| > 0$, its period $2\pi/|r| \to \infty$ as $r \to 0$. This is not allowed by the averaging method (1) used in [10]. In the case of $r = 0$, the function $\boldsymbol{p}_{\text{lf}}$ is then independent of τ.
2) The function $\boldsymbol{p}_{\text{hf}}(r\tau, \tau, \boldsymbol{e}_{\text{err}}, \boldsymbol{e}_{\text{err,I}})$ is 2π-periodic in τ for $r = 0$. If $|r| > 0$ and it is rational, the function $\boldsymbol{p}_{\text{hf}}$ is also periodic, since we can always find another time scale τ/m with an integer m such that any linear combination of $r\tau$ and τ is an integer multiple of τ/m. In this case, the function $\boldsymbol{p}_{\text{hf}}$ is $2\pi m$-periodic in τ. However, the period $2\pi m \to \infty$ as $r \to 0$, which is not allowed by the averaging method (1) used in [10]. If r is irrational, such integer m does not exist, which means $\boldsymbol{p}_{\text{hf}}$ is almost periodic in τ.
3) If the energy reference is given by the constant $\boldsymbol{E}$, then $\boldsymbol{p}_{\text{ref}}(r\tau, \tau) = \boldsymbol{0}$. If the energy reference is given by a stationary operating regime, as will be shown in Section IV-D, the function $\boldsymbol{p}_{\text{ref}}$ equals the function $\boldsymbol{p}_{\text{hf}}$ at vanishing error state. In this case, the properties of $\boldsymbol{p}_{\text{hf}}$ discussed in the previous point are valid for $\boldsymbol{p}_{\text{ref}}$.

To sum up, in lf-mode, the system (14) is considered to be almost periodic rather than periodic. Therefore, it is the general averaging (4) rather than averaging (1) used in [10] that contributes to the analysis in lf-mode.

After achieving the system (14) in the form of (5), the next step is to use general averaging (4) to derive an time-invariant average system where the controller design is carried out. However, before the general averaging process, it should be pointed out that the condition

$$\boldsymbol{p}_{\text{lf}} = \boldsymbol{0} \tag{15}$$

should hold. This can be explained in two different aspects. On one hand, from a mathematical viewpoint, since the norm of the antiderivative of the function $\boldsymbol{p}_{\text{lf}}$ w.r.t. τ is inversely proportional to $|r|$, it is possible that the limit defined in (4) does not exist as $r \to 0$. On the other hand, from a viewpoint of engineering, the power term $\boldsymbol{p}_{\text{lf}}$ leads to energy ripples with undesired large amplitudes when the frequency is extremely small, as pointed out in [5], [7], [31], [32], and [44]. The condition (15) means to compensate all powers or energy ripples at low frequency. Besides, the general average of $\boldsymbol{p}_{\text{hf}}$ and $\boldsymbol{p}_{\text{ref}}$ is zero since they are almost periodic in τ, as discussed in the text between (14) and (15). Therefore, the general averaging of the right-hand side of (14) reads

$$\begin{aligned}\lim_{T\to\infty} \frac{1}{T} \int_0^T & \left[\boldsymbol{p}_{\text{dc}}\left(\boldsymbol{e}_{\text{err}}, \boldsymbol{e}_{\text{err,I}}\right) + \boldsymbol{0}\right. \\ & \left. + \boldsymbol{p}_{\text{hf}}\left(r\tau, \tau, \boldsymbol{e}_{\text{err}}, \boldsymbol{e}_{\text{err,I}}\right) - \boldsymbol{p}_{\text{ref}}\left(r\tau, \tau\right)\right] \mathrm{d}\tau \\ & = \boldsymbol{p}_{\text{dc}}\left(\boldsymbol{e}_{\text{err}}, \boldsymbol{e}_{\text{err,I}}\right) \end{aligned} \tag{16a}$$

$$\lim_{T\to\infty} \frac{1}{T} \int_0^T \boldsymbol{e}_{\text{err}} \mathrm{d}\tau = \boldsymbol{e}_{\text{err}}. \tag{16b}$$

Notice that the states $\boldsymbol{e}_{\text{err}}$ and $\boldsymbol{e}_{\text{err,I}}$ are considered as time-independent while performing the integral, see Section II-A. As a result, the average system

$$\frac{\mathrm{d}}{\mathrm{d}\tau}\overline{\boldsymbol{e}}_{\text{err}} = \varepsilon \boldsymbol{p}_{\text{dc}}\left(\overline{\boldsymbol{e}}_{\text{err}}, \overline{\boldsymbol{e}}_{\text{err,I}}\right), \quad \frac{\mathrm{d}}{\mathrm{d}\tau}\overline{\boldsymbol{e}}_{\text{err,I}} = \varepsilon \overline{\boldsymbol{e}}_{\text{err}} \tag{17}$$

is obtained which corresponds to the standard average system form (6). Here, the state is represented by $(\overline{\boldsymbol{e}}_{\text{err}}^{\text{T}} \quad \overline{\boldsymbol{e}}_{\text{err,I}}^{\text{T}})^{\text{T}}$ in order to distinguish from $(\boldsymbol{e}_{\text{err}}^{\text{T}} \quad \boldsymbol{e}_{\text{err,I}}^{\text{T}})^{\text{T}}$ for the original system (14).

Since $\boldsymbol{p}_{\text{dc}}$ in (17) is independent of ε, by means of the definition $\varepsilon = 1/\omega_{\text{cm}}$, the average system (17) can be rewritten as

$$\dot{\overline{\boldsymbol{e}}}_{\text{err}} = \boldsymbol{p}_{\text{dc}}\left(\overline{\boldsymbol{e}}_{\text{err}}, \overline{\boldsymbol{e}}_{\text{err,I}}\right), \qquad \dot{\overline{\boldsymbol{e}}}_{\text{err,I}} = \overline{\boldsymbol{e}}_{\text{err}}. \tag{18}$$

The average system (18) uses the same time scale as the original energy control system (12), and thus, this rewriting helps comparing the solution of the two systems in the same t-scale, as will be seen in Fig. 5 in Section IV-E. The change of time-variable has no effect on the state variable, and thus, a feasible controller which leads to an exponential stability of the origin of the t-scaled system (18) will also guarantee a stability of the same art for the τ-scaled system (17). Therefore, in the following sub-section, energy controller candidates will be found at the t-scaled system (18).

B. Design at Average System

Due to the strong coupling [17], [18] of the energy model (8), some current coefficients appear in $\boldsymbol{p}_{\text{lf}}$ and $\boldsymbol{p}_{\text{dc}}$ at the same time and influence the dynamics w.r.t. different transformed energies, as can be easily noticed in (13). In order to avoid an elaborate "recursive" or "iterative" design procedure, we will follow a "single-run" design approach, in which the controller design and the coefficient design for compensation of ripples at low frequency will be considered together. First, the complete conditions w.r.t. all transformed energies will be derived, in which the conditions (20a), (20b), and (22) for e_{s0} and $\underline{e}_s$ will be discussed first in order to specify some current coefficients which simplifies the derivation of the conditions (23), (24) for e_{d0} and $\underline{e}_d$. Second, two different solutions, i.e., a simple choice (similar to [5]) and an optimization, to fulfill the conditions will be given after a short summary of the derived conditions.

By an appropriate choice of $\boldsymbol{p}_{\text{dc}}$, the system (18) can obey the linear error dynamics

$$\dot{\overline{\boldsymbol{e}}}_{\text{err}} = -k_{\text{P,e}}\overline{\boldsymbol{e}}_{\text{err}} - k_{\text{I,e}}\overline{\boldsymbol{e}}_{\text{err,I}} \qquad \dot{\overline{\boldsymbol{e}}}_{\text{err,I}} = \overline{\boldsymbol{e}}_{\text{err}} \tag{19}$$

which guarantees that the origin is globally exponentially stable if $k_{\text{P,e}} > 0$, $k_{\text{I,e}} > 0$. As in [10], the relation $k_{\text{I,e}} = k_{\text{P,e}}^2/2$ is chosen in order to keep a good compromise between the rapidity and the overshoot of the solution of (19) [45]. Substituting the error dynamics (19) into the system (18) leads to

$$\begin{aligned} 0 = {} & k_{\text{P,e}}\overline{e}_{s0,\text{err}} + k_{\text{I,e}}\overline{e}_{s0,\text{err,I}} \\ & + V_{\text{DC}}^{[0,0]} I_{s0}^{[0,0]}(\cdot,\cdot) - \text{Re}\left(\underline{V}_y^{[1,0]*}\underline{I}^{[1,0]}\right) \end{aligned} \tag{20a}$$

$$0 = k_{\text{P,e}}\underline{\overline{e}}_{s,\text{err}} + k_{\text{I,e}}\underline{\overline{e}}_{s,\text{err,I}} + \underline{I}_s^{[0,0]}(\cdot,\cdot)\, V_{\text{DC}}^{[0,0]} \tag{20b}$$

$$0 = k_{\text{P,e}}\overline{e}_{d0,\text{err}} + k_{\text{I,e}}\overline{e}_{d0,\text{err,I}}$$

$$- 2 \sum_{n\in\mathbb{N}_{\rm cm}} \left(\underline{I}_{s0}^{[0,n]}(\cdot,\cdot)\, \underline{V}_{y0}^{[0,n]*} + \underline{I}_{s0}^{[0,n]*}(\cdot,\cdot)\, \underline{V}_{y0}^{[0,n]} \right)$$
$$- \mathrm{Re}\left(\underline{V}_{y}^{[1,0]*} \underline{I}_{s}^{[1,0]}(\cdot,\cdot) \right) \tag{20c}$$

$$0 = k_{\mathrm{P,e}} \underline{\overline{e}}_{d,\mathrm{err}} + k_{\mathrm{I,e}} \underline{\overline{e}}_{d,\mathrm{err,I}}$$
$$- 2 \sum_{n\in\mathbb{N}_{\rm cm}} \left(\underline{I}_{s}^{[0,-n]}(\cdot,\cdot)\, \underline{V}_{y0}^{[0,n]} + \underline{I}_{s}^{[0,n]}(\cdot,\cdot)\, \underline{V}_{y0}^{[0,n]*} \right)$$
$$- \underline{I}_{s}^{[-1,0]*}(\cdot,\cdot)\, \underline{V}_{y}^{[1,0]*} - 2\underline{I}_{s0}^{[1,0]*}(\cdot,\cdot)\, \underline{V}_{y}^{[1,0]}. \tag{20d}$$

This means, all current coefficients which do not appear in (20) will no longer be considered as candidates of the controller output. Hence, their error dependency will be dropped in the following. In this case, the condition (15) leads to

$$0 = \sum_{\substack{n\in\mathbb{Z}^+\setminus\{1\},\\ |n\omega_{\rm m}|<\omega_{\rm cm}}} V_{\rm DC}^{[0,0]} \left(\underline{I}_{s0}^{[n,0]} \mathrm{e}^{jn\omega_{\rm m}t} + \underline{I}_{s0}^{[n,0]*} \mathrm{e}^{-jn\omega_{\rm m}t} \right)$$
$$+ V_{\rm DC}^{[0,0]} \left(\underline{I}_{s0}^{[1,0]}(\cdot,\cdot)\, \mathrm{e}^{j\omega_{\rm m}t} + \underline{I}_{s0}^{[1,0]*}(\cdot,\cdot)\, \mathrm{e}^{-j\omega_{\rm m}t} \right) \tag{21a}$$

$$0 = \sum_{n\in\{-1,1\}} V_{\rm DC}^{[0,0]} \underline{I}_{s}^{[n,0]}(\cdot,\cdot)\, \mathrm{e}^{jn\omega_{\rm m}t}$$
$$+ \sum_{n\in\mathbb{Z}\setminus\{0,-1,1\},|n\omega_{\rm m}|<\omega_{\rm cm}} V_{\rm DC}^{[0,0]} \underline{I}_{s}^{[n,0]} \mathrm{e}^{jn\omega_{\rm m}t}$$
$$- \underline{V}_{y}^{[1,0]*} \underline{I}^{[1,0]*} \mathrm{e}^{-j2\omega_{\rm m}t} \tag{21b}$$

which are derived by $p_{\mathrm{lf,es}0} = 0$ and $\underline{p}_{\mathrm{lf,es}} = 0$, respectively. It is obvious that all coefficients of i_{s0} and $\underline{i}_s$ which appear in (21), except for $\underline{I}_s^{[-2,0]}$, must be zero since they introduce powers at different low frequencies which cannot be compensated. Therefore, condition (21b) leads to

$$0 = V_{\rm DC}^{[0,0]} \underline{I}_{s}^{[-2,0]} - \underline{V}_{y}^{[1,0]*} \underline{I}^{[1,0]*}. \tag{22}$$

At the same time, (20c) and (20d) are simplified as follows:

$$0 = - 2 \sum_{n\in\mathbb{N}_{\rm cm}} \left(\underline{I}_{s0}^{[0,n]}(\cdot,\cdot)\, \underline{V}_{y0}^{[0,n]*} + \underline{I}_{s0}^{[0,n]*}(\cdot,\cdot)\, \underline{V}_{y0}^{[0,n]} \right)$$
$$+ k_{\mathrm{P,e}} \underline{\overline{e}}_{d0,\mathrm{err}} + k_{\mathrm{I,e}} \underline{\overline{e}}_{d0,\mathrm{err,I}} \tag{23a}$$

$$0 = - 2 \sum_{n\in\mathbb{N}_{\rm cm}} \left(\underline{I}_{s}^{[0,-n]}(\cdot,\cdot)\, \underline{V}_{y0}^{[0,n]} + \underline{I}_{s}^{[0,n]}(\cdot,\cdot)\, \underline{V}_{y0}^{[0,n]*} \right)$$
$$+ k_{\mathrm{P,e}} \underline{\overline{e}}_{d,\mathrm{err}} + k_{\mathrm{I,e}} \underline{\overline{e}}_{d,\mathrm{err,I}}. \tag{23b}$$

Considering the analysis above and avoiding redundant current harmonics which lead to powers that cannot be compensated, the rest part of the condition (15), i.e., $p_{\mathrm{lf,ed}0} = 0$ and $\underline{p}_{\mathrm{lf,ed}} = 0$, leads to

$$0 = - 4 \sum_{n\in\mathbb{N}_{\rm cm}} \left(\underline{V}_{y0}^{[0,n]} \underline{I}_{s0}^{[3,-n]} + \underline{V}_{y0}^{[0,n]*} \underline{I}_{s0}^{[3,n]} \right)$$
$$- \underline{V}_{y}^{[1,0]} \underline{I}_{s}^{[-2,0]*} \tag{24a}$$

$$0 = - 4 \sum_{n\in\mathbb{N}_{\rm cm}} \left(\underline{V}_{y0}^{[0,n]} \underline{I}_{s0}^{[1,-n]} + \underline{V}_{y0}^{[0,n]*} \underline{I}_{s0}^{[1,n]} \right)$$
$$- \underline{V}_{y}^{[1,0]} \underline{I}_{s}^{[0,0]*}(\cdot,\cdot) \tag{24b}$$

$$0 = V_{\rm DC}^{[0,0]} \underline{I}^{[1,0]} - \underline{V}_{y}^{[1,0]*} \underline{I}_{s}^{[-2,0]*} - 2\underline{V}_{y}^{[1,0]} I_{s0}^{[0,0]}(\cdot,\cdot)$$
$$- 2 \sum_{n\in\mathbb{N}_{\rm cm}} \left(\underline{V}_{y0}^{[0,n]} \underline{I}_{s}^{[1,-n]} + \underline{V}_{y0}^{[0,n]*} \underline{I}_{s}^{[1,n]} \right) \tag{24c}$$

$$0 = - \underline{V}_{y}^{[1,0]*} \underline{I}_{s}^{[0,0]*}(\cdot,\cdot)$$
$$- 2 \sum_{n\in\mathbb{N}_{\rm cm}} \left(\underline{V}_{y0}^{[0,n]} \underline{I}_{s}^{[-1,-n]} + \underline{V}_{y0}^{[0,n]*} \underline{I}_{s}^{[-1,n]} \right). \tag{24d}$$

To sum up, the conditions (20a), (20b), and (23) must be satisfied for the controller design, while the conditions (22) and (24) which are derived from the condition (15) must be fulfilled for the compensation of ripples at low frequency. Notice that these derived conditions are also available for the case where the coefficient $\underline{V}_{y0}^{[0,n]}$ of the common-mode voltage is also used as controller output with error dependency (like in [46]), since the error state is regarded as time-independent while taking the general averaging (4). Similar as the idea in [10], [47], and [48], the constant coefficients of the common-mode voltage v_{y0} avoid any nonlinearity w.r.t. the degrees of freedom to be solved in (23) and (24) such that the design effort can be reduced substantially. It is obvious that $I_{s0}^{[0,0]}(\cdot,\cdot)$, $\underline{I}_{s}^{[0,0]}(\cdot,\cdot)$, and $\underline{I}_{s}^{[-2,0]}$ are the only choice to fulfill the conditions (20a), (20b), and (22), respectively, and the solution reads

$$I_{s0}^{[0,0]}(\cdot,\cdot) = \left(-k_{\mathrm{P,e}} \underline{\overline{e}}_{s0,\mathrm{err}} - k_{\mathrm{I,e}} \underline{\overline{e}}_{s0,\mathrm{err,I}}\right) / V_{\rm DC}^{[0,0]}$$
$$+ \mathrm{Re}\left(\underline{V}_{y}^{[1,0]*} \underline{I}^{[1,0]} \right) / V_{\rm DC}^{[0,0]} \tag{25a}$$

$$\underline{I}_{s}^{[0,0]}(\cdot,\cdot) = \left(-k_{\mathrm{P,e}} \underline{\overline{e}}_{s,\mathrm{err}} - k_{\mathrm{I,e}} \underline{\overline{e}}_{s,\mathrm{err,I}}\right) / V_{\rm DC}^{[0,0]} \tag{25b}$$

$$\underline{I}_{s}^{[-2,0]} = \underline{V}_{y}^{[1,0]*} \underline{I}^{[1,0]*} / V_{\rm DC}^{[0,0]}. \tag{25c}$$

However, more than one current coefficient can be used for each condition in (23) and (24). In other words, the subsystem (23), (24) is underdetermined and has infinite solutions. In the following, two solutions are derived.

The first one is a simple choice, where only one feasible current coefficient is used to fulfill each equality in (23) and (24). This leads to the controller (25a), (25b) and

$$\underline{I}_{s0}^{[0,1]}(\cdot,\cdot) = \left(k_{\mathrm{P,e}} \underline{\overline{e}}_{d0,\mathrm{err}} + k_{\mathrm{I,e}} \underline{\overline{e}}_{d0,\mathrm{err,I}}\right) / \left(4\underline{V}_{y0}^{[0,1]*}\right) \tag{26a}$$

$$\underline{I}_{s}^{[0,1]}(\cdot,\cdot) = \left(k_{\mathrm{P,e}} \underline{\overline{e}}_{d,\mathrm{err}} + k_{\mathrm{I,e}} \underline{\overline{e}}_{d,\mathrm{err,I}}\right) / \left(2\underline{V}_{y0}^{[0,1]*}\right) \tag{26b}$$

while the additional current harmonic coefficients for (15) read (25c) and

$$\underline{I}_{s0}^{[3,1]} = \underline{I}_{s}^{[-2,0]*} \underline{V}_{y}^{[1,0]} / \left(-4\underline{V}_{y0}^{[0,1]*}\right) \tag{27a}$$

$$\underline{I}_{s0}^{[1,1]} = - \underline{V}_{y}^{[1,0]} \underline{I}_{s}^{[0,0]*}(\cdot,\cdot) / \left(4\underline{V}_{y0}^{[0,1]*}\right) \tag{27b}$$

$$\underline{I}_{s}^{[1,1]} = \left(V_{\rm DC}^{[0,0]} \underline{I}^{[1,0]} - \underline{I}_{s}^{[-2,0]*} \underline{V}_{y}^{[1,0]*}\right) / \left(2\underline{V}_{y0}^{[0,1]*}\right)$$
$$- 2I_{s0}^{[0,0]}(\cdot,\cdot)\, \underline{V}_{y}^{[1,0]} / \left(2\underline{V}_{y0}^{[0,1]*}\right) \tag{27c}$$

$$\underline{I}_{s}^{[-1,1]} = - \underline{I}_{s}^{[0,0]*}(\cdot,\cdot)\, \underline{V}_{y}^{[1,0]*} / \left(2\underline{V}_{y0}^{[0,1]*}\right). \tag{27d}$$

This choice only cooperates with the fundamental component of the common-mode voltage v_{y0}, and is very similar as in [5] except for the harmonics with order -1 w.r.t. ω_{cm} in the circulating current in [5]. In the case of $\omega_{\mathrm{m}} = 0$, this variant is equivalent to the controller with the simple choice in [10] for dc-operation of MMC.

The second is an optimization, i.e., a quadratic programming problem with linear constraints. Inspired by [10], the objective function is given by the quadratic form

$$\begin{aligned} f_{\mathrm{obj}} = 4 &\left(\sum_{n\in\mathbb{N}_{\mathrm{cm}}} \left| \underline{I}_{s0}^{[0,n]}(\cdot,\cdot) \right|^2 + \sum_{\substack{n_1\in\{1,3\},\\ n_2\in\mathbb{N}_{\mathrm{cm}}}} \left| \underline{I}_{s0}^{[n_1,n_2]} \right|^2 \right) \\ &+ \sum_{n\in\mathbb{N}_{\mathrm{cm}}} \left(\left| \underline{I}_{s}^{[0,n]}(\cdot,\cdot) \right|^2 + \left| \underline{I}_{s}^{[0,-n]}(\cdot,\cdot) \right|^2 \right) \\ &+ \sum_{n_1\in\{-1,1\},n_2\in\mathbb{N}_{\mathrm{cm}}} \left(\left| \underline{I}_{s}^{[n_1,n_2]} \right|^2 + \left| \underline{I}_{s}^{[n_1,-n_2]} \right|^2 \right) \end{aligned} \tag{28}$$

and it is subjected to the constraints (23), (24) which are linear due to the constancy of the coefficient of the common-mode voltage. This problem is convex and the objective function (28) is nonnegative. According to the variable definition in [19], [35], the minimum of (28) leads to the smallest arm current RMS, when the MMC approaches a regime in which all current coefficients in (28) are constant. The solution of the problem leads to the optimized controller given by (25a), (25b), and

$$\underline{I}_{s0}^{[0,n]}(\cdot,\cdot) = \underline{V}_{y0}^{[0,n]} \frac{k_{\mathrm{P,e}}\overline{e}_{d0,\mathrm{err}} + k_{\mathrm{I,e}}\overline{e}_{d0,\mathrm{err,I}}}{A} \tag{29a}$$

$$\underline{I}_{s}^{[0,-n]}(\cdot,\cdot) = \underline{V}_{y0}^{[0,n]*} \frac{k_{\mathrm{P,e}}\underline{\overline{e}}_{d,\mathrm{err}} + k_{\mathrm{I,e}}\underline{\overline{e}}_{d,\mathrm{err,I}}}{A} \tag{29b}$$

$$\underline{I}_{s}^{[0,n]}(\cdot,\cdot) = \underline{V}_{y0}^{[0,n]} \frac{k_{\mathrm{P,e}}\underline{\overline{e}}_{d,\mathrm{err}} + k_{\mathrm{I,e}}\underline{\overline{e}}_{d,\mathrm{err,I}}}{A} \tag{29c}$$

while the optimized additional current harmonic coefficients for (15) read (25c) and

$$\underline{I}_{s0}^{[3,-n]} = -\underline{V}_{y0}^{[0,n]*}\underline{I}_{s}^{[-2,0]*}\underline{V}_{y}^{[1,0]}/(2A) \tag{30a}$$

$$\underline{I}_{s0}^{[3,n]} = -\underline{V}_{y0}^{[0,n]}\underline{I}_{s}^{[-2,0]*}\underline{V}_{y}^{[1,0]}/(2A) \tag{30b}$$

$$\underline{I}_{s0}^{[1,-n]} = -\underline{V}_{y0}^{[0,n]*}\underline{I}_{s}^{[0,0]*}(\cdot,\cdot)\,\underline{V}_{y}^{[1,0]}/(2A) \tag{30c}$$

$$\underline{I}_{s0}^{[1,n]} = -\underline{V}_{y0}^{[0,n]}\underline{I}_{s}^{[0,0]*}(\cdot,\cdot)\,\underline{V}_{y}^{[1,0]}/(2A) \tag{30d}$$

$$\begin{aligned} \underline{I}_{s}^{[1,-n]} = {} & \underline{V}_{y0}^{[0,n]*}\left(V_{\mathrm{DC}}^{[0,0]}\underline{I}^{[1,0]} - \underline{I}_{s}^{[-2,0]*}\underline{V}_{y}^{[1,0]*}\right)/A \\ & - 2\underline{V}_{y0}^{[0,n]*}\underline{V}_{y}^{[1,0]}I_{s0}^{[0,0]}(\cdot,\cdot)/A \end{aligned} \tag{30e}$$

$$\begin{aligned} \underline{I}_{s}^{[1,n]} = {} & \underline{V}_{y0}^{[0,n]}\left(V_{\mathrm{DC}}^{[0,0]}\underline{I}^{[1,0]} - \underline{I}_{s}^{[-2,0]*}\underline{V}_{y}^{[1,0]*}\right)/A \\ & - 2\underline{V}_{y0}^{[0,n]}\underline{V}_{y}^{[1,0]}I_{s0}^{[0,0]}(\cdot,\cdot)/A \end{aligned} \tag{30f}$$

$$\underline{I}_{s}^{[-1,-n]} = -\underline{V}_{y0}^{[0,n]*}\underline{I}_{s}^{[0,0]*}(\cdot,\cdot)\,\underline{V}_{y}^{[1,0]*}/A \tag{30g}$$

$$\underline{I}_{s}^{[-1,n]} = -\underline{V}_{y0}^{[0,n]}\underline{I}_{s}^{[0,0]*}(\cdot,\cdot)\,\underline{V}_{y}^{[1,0]*}/A \tag{30h}$$

with $n \in \mathbb{N}_{\mathrm{cm}}$ and $A = 4\sum_{m\in\mathbb{N}_{\mathrm{cm}}} |\underline{V}_{y0}^{[0,m]}|^2$. Unlike the ones in [5] and [7] which only utilize one or a part of feasible current harmonics, by cooperating with all harmonics in the common-mode voltage v_{y0}, this variant enables all feasible current harmonic coefficients to fulfill the conditions (23) and (24). Notice that the number of current harmonics varies according to the common-mode voltage. Unlike [18] and [49] which focused on optimizing controller parameters, the solution (29) and (30) leads to an optimized distribution of the PI-control effort in (23) and the effort in (24) for compensating ripples at low frequency to all feasible current harmonics, such that the minimum of the objective function (28) is achieved. Although (29), (30) consider the energy control transient by regarding the energy error dependency, by substituting $\mathbf{0}$ for all energy errors, the current coefficients in (29) and (30) will generate an optimized regime with minimal arm current RMS, as will be discussed in Section IV-D. In the case of $\omega_{\mathrm{m}} = 0$, this variant is equivalent to the optimized controller in [10] for dc-operation of MMC.

C. Energy Control System

Using the two candidates above with the substitution $\overline{\boldsymbol{e}}_{\mathrm{err}} = \boldsymbol{e}_{\mathrm{err}}$ and $\overline{\boldsymbol{e}}_{\mathrm{err,I}} = \boldsymbol{e}_{\mathrm{err,I}}$, the energy control system in Fig. 4 is derived as follows.

1) The switch $\mathrm{S}_{\mathrm{coeff}}$ indicates the two options introduced in Section IV-B for energy control and compensation of ripples at low frequency, i.e., the simple choice (similar to [5]) cooperating only with the fundamental component of the common-mode voltage and the optimization utilizing all feasible current harmonics in cooperation with all harmonics in the common-mode voltage.
2) The switch $\mathrm{S}_{\mathrm{vy0}}$ selects between the two options in Section III-A for the common-mode voltage, i.e., $v_{y0}^{\mathrm{1st+3\,rd}}$ [6, Sec. IV-B] and the approximated trapezoidal waveform v_{y0}^{trpz} with up to 7th harmonic w.r.t. ω_{cm}.
3) The switch $\mathrm{S}_{\mathrm{ref}}$ indicates the two options for energy reference, i.e., the constant $\boldsymbol{E}$ [17], [34] or a calculated stationary operating regime $\boldsymbol{e}_{\mathrm{rgm}}$ [5]. The design of the regime will be illustrated in the following subsection, by means of the condition (7).

D. Design of Stationary Operating Regimes

According to (7), the stationary operating regime $\boldsymbol{e}_{\mathrm{rgm}}$ can be designed such that the origin of the energy error is an equilibrium point of the energy control system (12), which means that the remaining error vanishes. This leads to $\boldsymbol{p}_{\mathrm{ref}}(\omega_{\mathrm{m}}t, \omega_{\mathrm{cm}}t) = \boldsymbol{p}_{\mathrm{hf}}(\omega_{\mathrm{m}}t, \omega_{\mathrm{cm}}t, \mathbf{0}, \mathbf{0})$ which is derived from (12) with $\boldsymbol{e}_{\mathrm{err}} = \mathbf{0}$, $\boldsymbol{e}_{\mathrm{err,I}} = \mathbf{0}$, the condition (15), and the system (18) designed as the linear dynamics (19). In other words, a feasible stationary operating regime can be obtained by integrating the energy model (8), where the corresponding current injection is determined by the energy controller and the additional current harmonics for (15) with vanishing energy error, and the general average of the regime $\boldsymbol{e}_{\mathrm{rgm}}$ is set to the constant $\boldsymbol{E}$.

This method extends the one in [10] for MMC dc-operation to lf-mode in this text. Generally speaking, a stationary operating

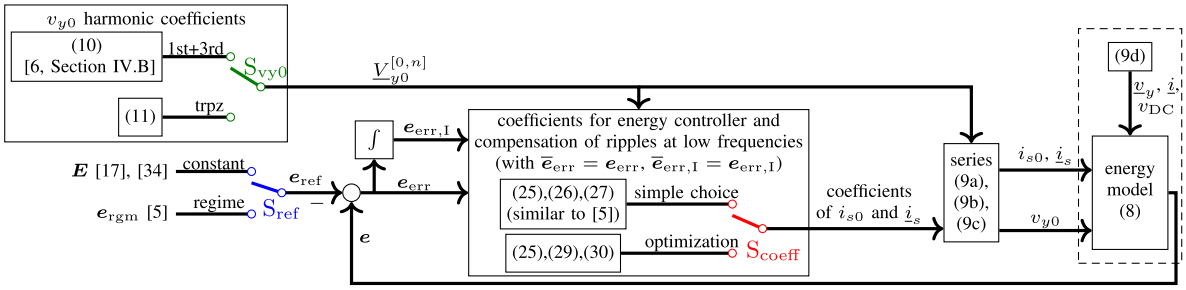

Fig. 4. Energy control system for lf-mode. The implementation of the part in the dashed block for the experiments will be explained in Section V-A.

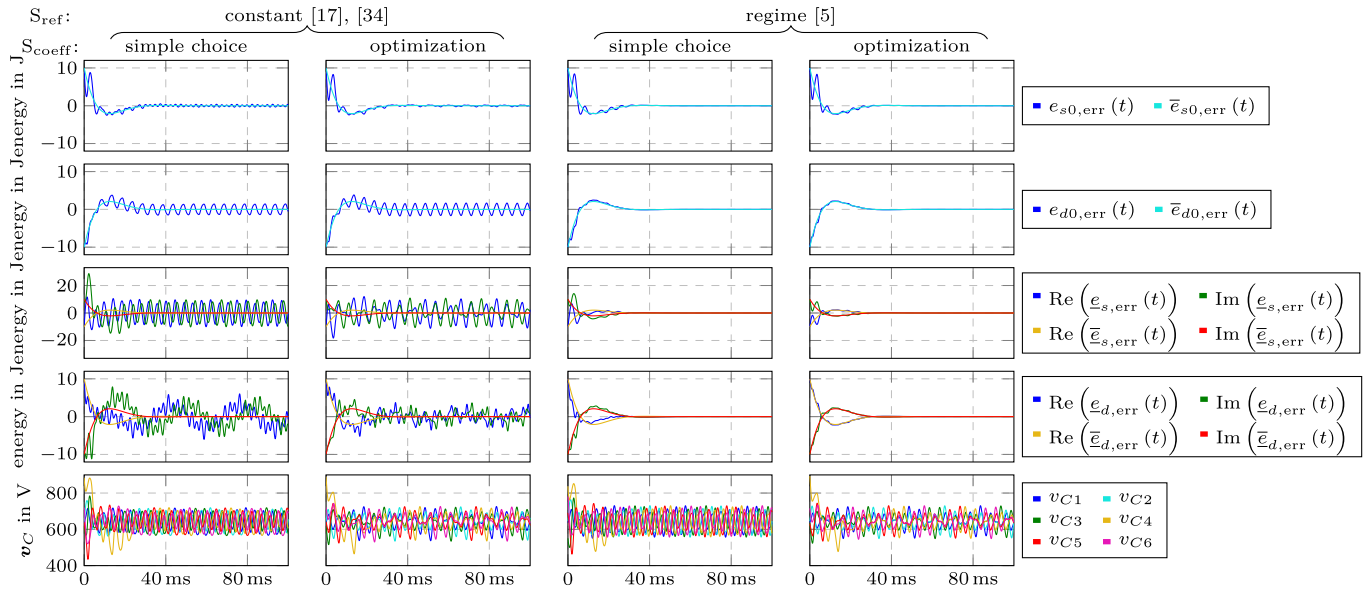

Fig. 5. Simulative verification of the stability of the energy control system in Fig. 4, with the energy error $e_{err}(t)$ of the proposed energy control system in Fig. 4 and the solution $\overline{e}_{err}(t)$ of the associated dynamics (19) of the average system. The common-mode voltage is given by $v_{y0}^{1st+3rd}$ (Fig. 3, red. Also see S_{vy0}: 1st+3 rd in Fig. 4.). Settings: $\underline{I}^{[1,0]} = 8\,A$, $V_{DC}^{[0,0]} = 600\,V$, $\omega_m = 2\pi \cdot 30\,rad/s$, $\omega_{cm} = 2\pi \cdot 200\,rad/s$, $k_{P,e} = 250\,Hz$, $k_{I,e} = k_{P,e}^2/2$.

regime can be designed in such a way that the chosen current and voltage injections to the energy model (8) will keep the average value of the energies constant, as the idea mentioned in [19] and [21]. The method in this text aims on finding a stationary operating regime to eliminate the remaining energy control error of the system in Fig. 4, and it shows no contradiction to the conventional idea in [19] and [21] by using the substitution $e_{err} = 0$, $e_{err,I} = 0$ into (12) to guarantee a constant average value of the energies.

As mentioned in Section IV-B, following the method above, the optimization leads to an optimized regime utilizing all feasible current harmonics in cooperation with all harmonics in common-mode voltage to achieve minimal arm current RMS. Notice that the number of current harmonics and thus, the waveform of the circulating current is determined by the common-mode voltage, confirmed by (30). Thus, among the steady states in [6] and [31] and the proposed optimized regime, the difference of the circulating currents is analogous to that of the common-mode voltages described in Section III-A. In the case of $v_{y0}^{1st+3rd}$ as the common-mode voltage, the optimized regime utilizes the same distribution of the compensation effort to the arm currents, and thus the same minimum point in terms of arm current RMS as [7, Strategy II], while the current injection in [6, Sec. IV-B] cooperating with the same common-mode voltage does not consider any optimization.

E. Stability of the Energy Control System

The system in Fig. 4 is the proposed energy control system for lf-mode, covering the one in [10, Fig. 4] for MMC dc-operation ($\omega_m = 0$) as a specific case. According to Theorem 1 in Appendix, the stability of this control system can be stated as follows:[1] For a sufficiently large predetermined frequency ω_{cm} and with the same initial values, the error $(e_{err}^T(t) \quad e_{err,I}^T(t))^T$ of the proposed energy control system in Fig. 4 lies (for $\forall t \in [0, \infty)$) in a neighborhood of the solution $(\overline{e}_{err}^T(t) \quad \overline{e}_{err,I}^T(t))^T$ of the dynamics (19) of the corresponding average system which

[1] The required convergence function in the condition C2 and C3 can be chosen as $f_{cvg}(T) = \frac{1}{T+1}$, confirmed by [29].

converges globally and exponentially to $\mathbf{0}$, and the remaining error vanishes when the energy reference is given by the regime $\boldsymbol{e}_{\text{rgm}}$. In other words: By means of the energy control system in Fig. 4, for a sufficiently large predetermined frequency ω_{cm}, the MMC energy $\boldsymbol{e}(t)$ converges globally to a neighborhood of the constant reference $\boldsymbol{E}$, or it tracks the calculated regime $\boldsymbol{e}_{\text{rgm}}$.

Although the range of ω_{cm} for the stabilization of the control system is hard to determine due to the complexity of the proof of Theorem 1 [29], the choice $\varepsilon = \frac{1}{\omega_{\text{cm}}}$ offers the possibility to decrease ε for stabilizing the energy control system by increasing the predetermined frequency ω_{cm}, where the restriction should be the pulse width modulation (PWM) frequency and the current control accuracy [6], [37].

Simulative verification of the stability can be found in Fig. 5. As shown by the first four rows, the energy error $\boldsymbol{e}_{\text{err}}(t)$ always lies in a neighborhood of the solution $\overline{\boldsymbol{e}}_{\text{err}}(t)$ of the associated dynamics (19) of the average system, which confirms the stability of the energy control system in Fig. 4 at the chosen predetermined frequency $\omega_{\text{cm}} = 2\pi \cdot 200\,\text{rad/s}$. As confirmed by the theoretical conclusions above, the remaining energy error vanishes only for the regime as energy reference (in the two rightmost columns). Notice that the ripples of the equivalent cell capacitor voltage $\boldsymbol{v}_C$ in the last row are caused by different reasons: For the constant energy reference in the two leftmost columns, the ripples in $\boldsymbol{v}_C$ are caused by the remaining energy control errors, while the ripples of $\boldsymbol{v}_C$ in the rightmost two columns correspond to the designed energy ripples in the stationary regime. A dedicate comparison between the two kinds of energy reference will be given by the experiments in Section V.

To sum up, for a sufficiently large predetermined frequency ω_{cm}, the MMC energy $\boldsymbol{e}(t)$ converges globally to a neighborhood of the constant reference $\boldsymbol{E}$, or it tracks the calculated regime $\boldsymbol{e}_{\text{rgm}}$. The validity and stability of a constant reference for the instantaneous MMC energies in lf-mode is verified theoretically, which is missing in the state-of-art research. Unlike [7], [27], and[30] which only provide a region of attraction in an uncertain small neighborhood of a stationary operating regime/point, the energy control system in Fig. 4 is proved to be globally stable.

V. Experiments

Although Theorem 1 in Appendix provides a rigorous global stability for the energy control system in Fig. 4, it is difficult to analyze the arm currents and the cell capacitor voltages directly, since Theorem 1 cannot offer the exact solution of the error dynamics. Thus, it is more efficient to explore the effect of the energy control system on the performance of the MMC by experiments. As will be shown in this section, the experiments will verify the stability of the energy control system in Fig. 4, and also provide comparisons between the different options w.r.t. the common-mode voltage, the energy reference, and the energy controller and compensation of ripples at low frequency, as represented by the three switches in Fig. 4.

A. Testbench Settings

The configuration of the experimental system is shown in Fig. 1, where a permanent magnet synchronous machine (PMSM) is taken as the ac machine. The dc link capacitor voltage is controlled by means of a grid side active rectifier. For the implementation of the part in dashed block in Fig. 4, the energy model is replaced by an MMC with current control and PWM, as in [19]. As indicated by Fig. 2, the controller for $\underline{i}$ receives the reference from the speed control of the ac machine and generates $\underline{v}_y$ for the modulation, while the signal v_{DC} is obtained from the dc link voltage measurement.

TABLE I
Test Bench Settings for the lf-Mode

Parameter	Value
Number of cells per arm	6
Cell capacitor	360 µF
Arm inductor	1.2 mH
$\boldsymbol{E}$	$(50\,\text{J}, 0, 0, 0, 0, 0)^{\text{T}}$
PWM frequency	4884 Hz, method A 4 [14], leading to an average switching frequency of 857 Hz.
v_{DC}	Around 600 V (provided by a dc link capacitor which is controlled by a grid side rectifier)
ω_{cm}	$2\pi \cdot \frac{4884}{24}\text{rad/s} = 2\pi \cdot 203.5\,\text{rad/s}$
$k_{\text{P,e}}$ and $k_{\text{I,e}}$	$k_{\text{P,e}} = 250\,\text{Hz}$, $k_{\text{I,e}} = k_{\text{P,e}}^2/2$

The test bench parameters are given in Table I.As indicated by Section I including Fig. 2, keeping PWM frequency sufficiently large is necessary for well-accomplished current control and cell voltage balancing stage, which is the requirement/precondition of using the energy model (8) for the design in the energy control stage. According to the conclusion in Section IV-E, the predetermined frequency ω_{cm} needs to be large enough to guarantee the stability of the proposed energy control system. However, this frequency must be restricted in order to achieve a good controllability of the currents [6], [37]. Therefore, the predetermined high frequency ω_{cm} is chosen as $2\pi \cdot \frac{4884}{24}\text{rad/s} = 2\pi \cdot 203.5\,\text{rad/s}$ which ensures 24 samplings within each period w.r.t. ω_{cm}. The controller parameter $k_{\text{P,e}} = 250\,\text{Hz}$ has the same value as the settings for Fig. 5, which means that the transient of the proposed energy dynamics ends within around 30 ms.

As illustrated in the paragraph before Section III-A, the condition $|n_1\omega_{\text{m}}| < \omega_{\text{cm}}$ is required in (9), with $\max(n_1) = 3$ in the designed variants. Thus, by choosing $\omega_{\text{cm}} = 2\pi \cdot 203.5\,\text{rad/s}$ in the experiments, the tested stator electrical frequency should not exceed $2\pi \cdot 203.5/3 \approx 2\pi \cdot 68\,\text{rad/s}$ (54.4% p.u.). Another factor that will limit the frequency range is the voltage reserve/margin. Due to the almost periodic characteristics in lf-mode, around $v_{\text{DC}}/2 - \max|v_{y0}| \approx 150\,\text{V}$ is left for machine EMF, current driving voltage, and margin for control transients and energy ripples, according to the current experimental settings.

The PMSM control bases on the classic field/rotor oriented control, e.g., in [5]. Due to the permanent magnet, the d-axis current reference is set to zero, while the q-axis current produces torque for the speed control. In contrast to [5], for an improved

TABLE II
PARAMETERS OF PMSM

Parameter	Value
Stator resistance	$R_\mathrm{s} = 0.59\,\Omega$
d,*q*-axis inductance	$L_\mathrm{d} = 17.8\,\mathrm{mH}, \quad L_\mathrm{q} = 12.5\,\mathrm{mH}$
Flux linkage of the permanent magnet	$\psi_\mathrm{d} = 0.313\,96\,\mathrm{V\,s}$
Total inertia	$J = 0.0303\,\mathrm{kgm}^2$
Number of pole pairs	$N_\mathrm{P} = 5$
Frictional coefficient	$f_\mathrm{frc} = 0.004\,07\,\mathrm{Nms/rad}$
Nominal value of ω_m	$2\pi{\cdot}125\,\mathrm{rad/s}$

speed control, the torque observer

$$\hat{x}_\mathrm{obs} = \frac{J}{N_\mathrm{P}}\omega_\mathrm{m} + k_\mathrm{obs}\hat{T}_\mathrm{L} \tag{31a}$$

$$\dot{\hat{x}}_\mathrm{obs} = \frac{3}{2}N_\mathrm{P}\left(\psi_\mathrm{d} + (L_\mathrm{d} - L_\mathrm{q})\,i_\mathrm{d}\right)i_\mathrm{q} - \frac{f_\mathrm{frc}}{N_\mathrm{P}}\omega_\mathrm{m} - \hat{T}_\mathrm{L} \tag{31b}$$

is designed according to the mechanical dynamics of the PMSM given by [50]

$$\frac{J}{N_\mathrm{P}}\dot{\omega}_\mathrm{m} = \frac{3}{2}N_\mathrm{P}\left(\psi_\mathrm{d} + (L_\mathrm{d} - L_\mathrm{q})\,i_\mathrm{d}\right)i_\mathrm{q} - \frac{f_\mathrm{frc}}{N_\mathrm{P}}\omega_\mathrm{m} - T_\mathrm{L}. \tag{32}$$

Here, $\hat{x}_\mathrm{obs}$ denotes the state of the observer, $\hat{T}_\mathrm{L}$ denotes the observer output, k_obs is a positive constant, T_L denotes the load torque, while the other parameters are given in Table II. The observer (31) and the model (32) lead to the dynamics

$$k_\mathrm{obs}\frac{\mathrm{d}}{\mathrm{d}t}\left(\hat{T}_\mathrm{L} - T_\mathrm{L}\right) + \left(\hat{T}_\mathrm{L} - T_\mathrm{L}\right) = 0 \tag{33}$$

when the load torque is constant, i.e. $\dot{T}_\mathrm{L} = 0$. The dynamics (33) means that the output $\hat{T}_\mathrm{L}$ converges exponentially to the load torque T_L, and a smaller k_obs leads to a faster convergence. The observer output $\hat{T}_\mathrm{L}$ is used as a feedforward signal to support the speed controller.

The real axis of the MMC ac side current $\underline{i}$ will be oriented to the q-axis, i.e. $\underline{I}^{[1,0]} = i_\mathrm{q} + ji_\mathrm{d}$. The absolute value of the reference $i_\mathrm{q,ref}$ is limited to 6 A in order to keep the amplitude of the arm currents within the safe operating area of the semiconductors. An anchor current controlled separately excited dc machine works as the mechanical load for the PMSM.

The experiments focus on the comparison among the different options in the energy control system, as represented by the switches $\mathrm{S_{ref}}$, $\mathrm{S_{vy0}}$, and $\mathrm{S_{coeff}}$ in Fig. 4. For this purpose, three performance indexes are defined as follows.

1) The maximal absolute value $I_{z,\max}$ among the six arm currents.
2) The RMS value $I_{z,\mathrm{rms,sum}}$ of the arm currents

$$I_{z,\mathrm{rms,sum}} = \sqrt{\frac{1}{T}\int_{\mathbb{T}}\sum_{n=1}^{6} i_{zn}^2\,\mathrm{d}t} \tag{34}$$

where i_{zn} for $n = 1,\ldots,6$ are the six arm currents, and T represents the length of the compact time interval $\mathbb{T}$.
3) The peak-to-peak value $v_{C,\mathrm{pp}}$ of the six equivalent cell capacitor voltages.

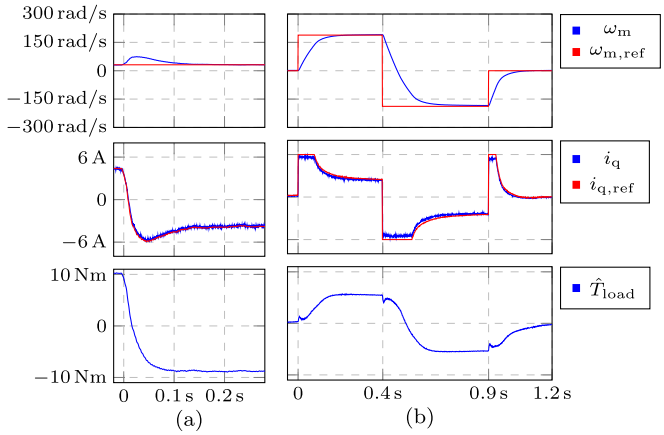

Fig. 6. Example of the behavior of the PMSM during the test process for (a) stability verification (b) performance at varying stator electrical frequency with the settings $\mathrm{S_{coeff}}$: optimization, $\mathrm{S_{ref}}$: regime, $\mathrm{S_{vy0}}$: trpz.

B. Experimental Results

1) Stability: In the computational verification of the stability shown in Fig. 5, the initial value of the energy errors are set to the same for all options of the energy control system. This is hard to achieve in the experiment due to the ripples of the MMC energies. Thus, in the experiments, an alternative process is chosen to verify the stability of the energy control system in Fig. 4, i.e., a load torque change is utilized to create an imbalance for the energy control system to react to, see Fig. 6(a) as an example of the behavior of PMSM. The load change at 0 s results in a speed control transient for only about 0.1 s, thanks to the torque observer which follows the new load torque fast, as shown in the first and the last row in Fig. 6(a). As a result, the MMC needs to enter a new stationary operation with different ac-side load currents, as shown in the second row.

The measured energy errors during this process are shown in Fig. 7. The results w.r.t. the simple choice (similar to [5]) for the energy control and compensation of powers at low frequency are given in the first row, while the results of the optimization with the two common-mode voltages are shown in the last two rows. The first column shows the results with the constant $\boldsymbol{E}$ as the reference for the instantaneous MMC energies [17], [34], while the second column represents the results w.r.t. the regime $\boldsymbol{e}_\mathrm{rgm}$ as the reference [5]. After the transient due to the load change, the energy error converges to the visible remaining error around $\mathbf{0}$ in the case of the constant reference $\boldsymbol{E}$ (left column), while the remaining control errors almost vanish in the case of the regime as reference (right column). Thus, the experimental results coincide well with the theoretical conclusions in Section IV-E. The effect of the different remaining control errors on the MMC performance will be explored by means of the measured arm currents and cell capacitor voltages in the following.

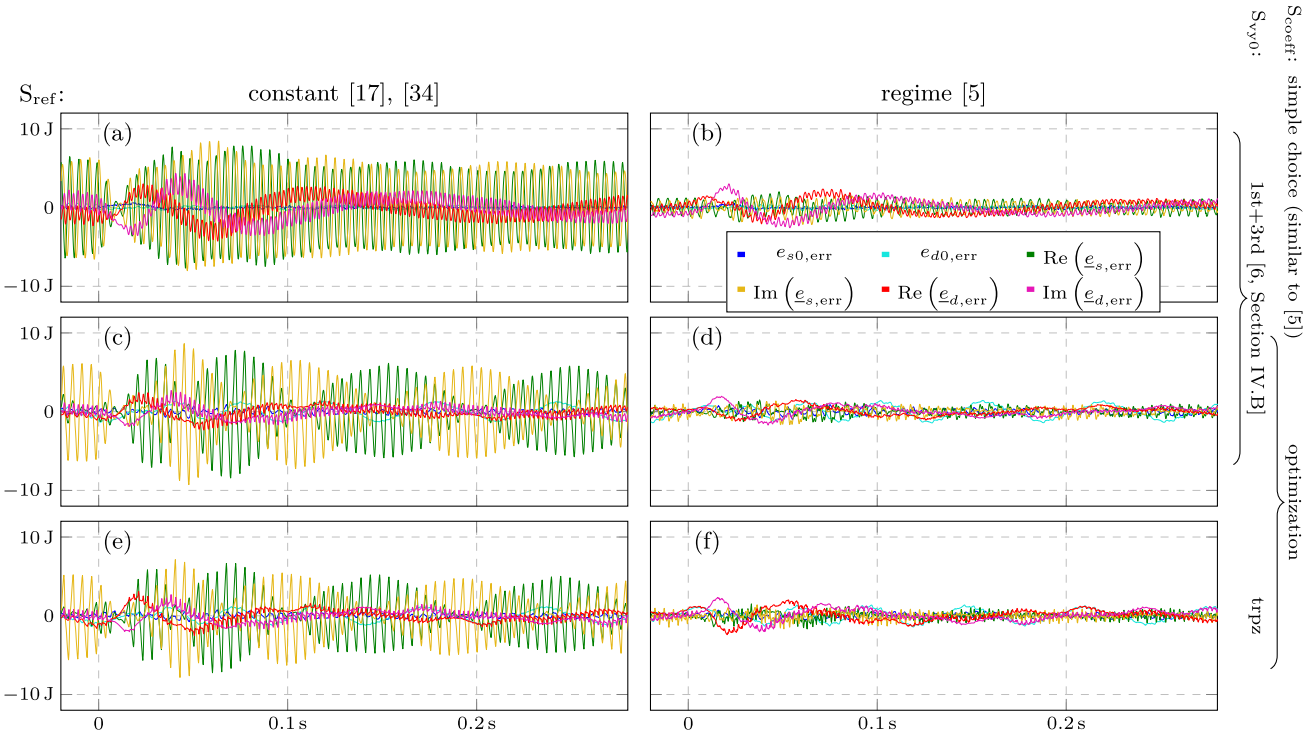

Fig. 7. Measurement results of the energy errors during the test process for stability verification shown in Fig. 6(a), at $\omega_{\mathrm{m}} = 2\pi \cdot 5\,\mathrm{Hz}$ (4% p.u.).

2) Stationary Performance: The stationary performance w.r.t. different options of the energy control system is compared by means of the results in Figs. 8 and 9 under the same stationary condition as in Fig. 6(a) after 0.2 s.

The subfigures have the same organization as in Fig. 7. The defined performance indexes for the subfigure (a) in the upper left corner are given by their values, while the indexes for the other subfigures (b)–(f) are given by a percentage compared to (a). As mentioned in Section IV-D, the results in (d) correspond to [7, Strategy II]. The results are illustrated as follows.

1) The two options for the energy reference are compared by means of (a), (c), (e) for constant reference $\boldsymbol{E}$ [17], [34] and (b), (d), (f) for regime as reference [5], respectively. As mentioned in Section IV-E, the ripples in the equivalent cell capacitor voltage $\boldsymbol{v}_C$ in the case of the constant energy reference $\boldsymbol{E}$ in (a), (c), (e) in Fig. 8 is caused by the remaining energy control errors, while the ripples of $\boldsymbol{v}_C$ in the case of regime as reference in (b), (d), (f) correspond to the energy ripples in the designed stationary regime. On the whole, the stationary operation resulting from the constant energy reference $\boldsymbol{E}$ [17], [34] is comparable to the designed regime as energy reference [5], except for larger peak arm current $I_{z,\max}$ caused by the constant reference $\boldsymbol{E}$ with the optimization.
2) The two options for the energy controller and compensation of ripples at low frequency are compared by means of (a), (b) for the simple choice (similar to [5]) and (c), (d) for the optimization, respectively. Compared with the simple choice, the optimization reduces the arm current RMS $I_{z,\mathrm{rms,sum}}$ significantly, and also reduces the peak arm current $I_{z,\max}$ in the case of regime as reference in (d).
3) The two options for the common-mode voltages are compared by means of (c), (d) for $v_{y0}^{1\mathrm{st}+3\,\mathrm{rd}}$ [6, Sec. IV-B], and (e), (f) for approximated trapezoidal waveform v_{y0}^{trpz}, respectively. With the optimization, at a cost of increased peak arm current $I_{z,\max}$, the approximated trapezoidal waveform v_{y0}^{trpz} leads to smaller arm current RMS $I_{z,\mathrm{rms,sum}}$ and significantly smaller peak-to-peak value $v_{C,\mathrm{pp}}$ of the equivalent cell capacitor voltage ripples, compared to $v_{y0}^{1\mathrm{st}+3\,\mathrm{rd}}$.
4) The results in (d)–(f) confirm the optimized stationary regime/operation generated by the optimization in cooperation with v_{y0}^{trpz} as an improvement of [7, Strategy II] in the sense of smaller arm current RMS and cell capacitor voltage fluctuation.

3) Performance at Varying Frequency: In order to explore the performance at varying stator electrical frequency which is not considered in the assumption of the analysis in Sections III and IV, the proposed energy control system is tested by a process with several speed reference steps. An example of the behavior of PMSM is given in Fig. 6(b). At 0 s, the reference $\omega_{\mathrm{m,ref}}$ of the electrical stator frequency steps from 0 to $2\pi{\cdot}30\,\mathrm{rad/s}$ which is 24% of its nominal value. At 0.4 s, the machine is controlled to accomplish a speed reversal from 24% to -24% of its nominal speed, while the speed reference steps back to zero at 0.9 s. The anchor current reference of the dc machine is proportional to the rotor speed, with 100% p.u. at the nominal rotor speed of PMSM, to provide a passive speed-dependent

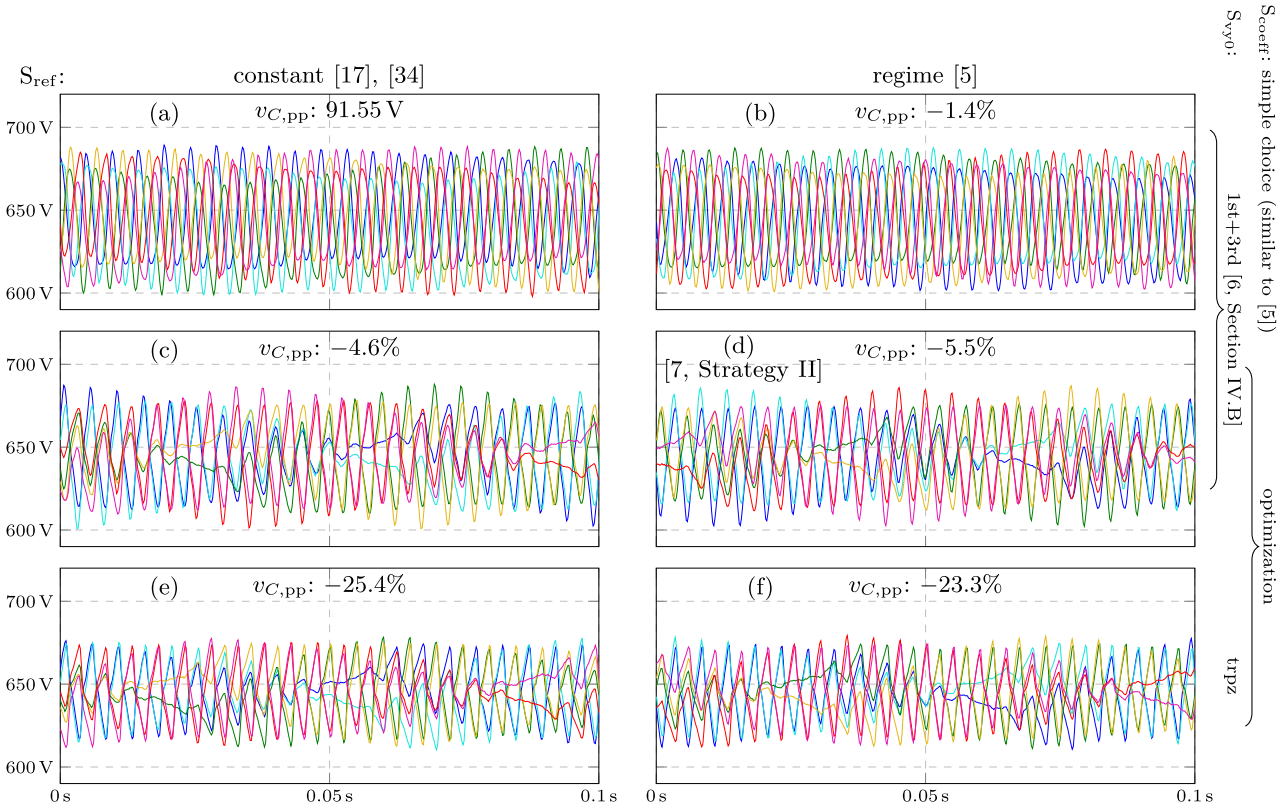

Fig. 8. Measurement results of the six equivalent cell capacitor voltages during the stationary operation at $\omega_\mathrm{m} = 2\pi \cdot 5\,\mathrm{Hz}$ (4% p.u.) and $i_\mathrm{q} = -3.7\,\mathrm{A}$.

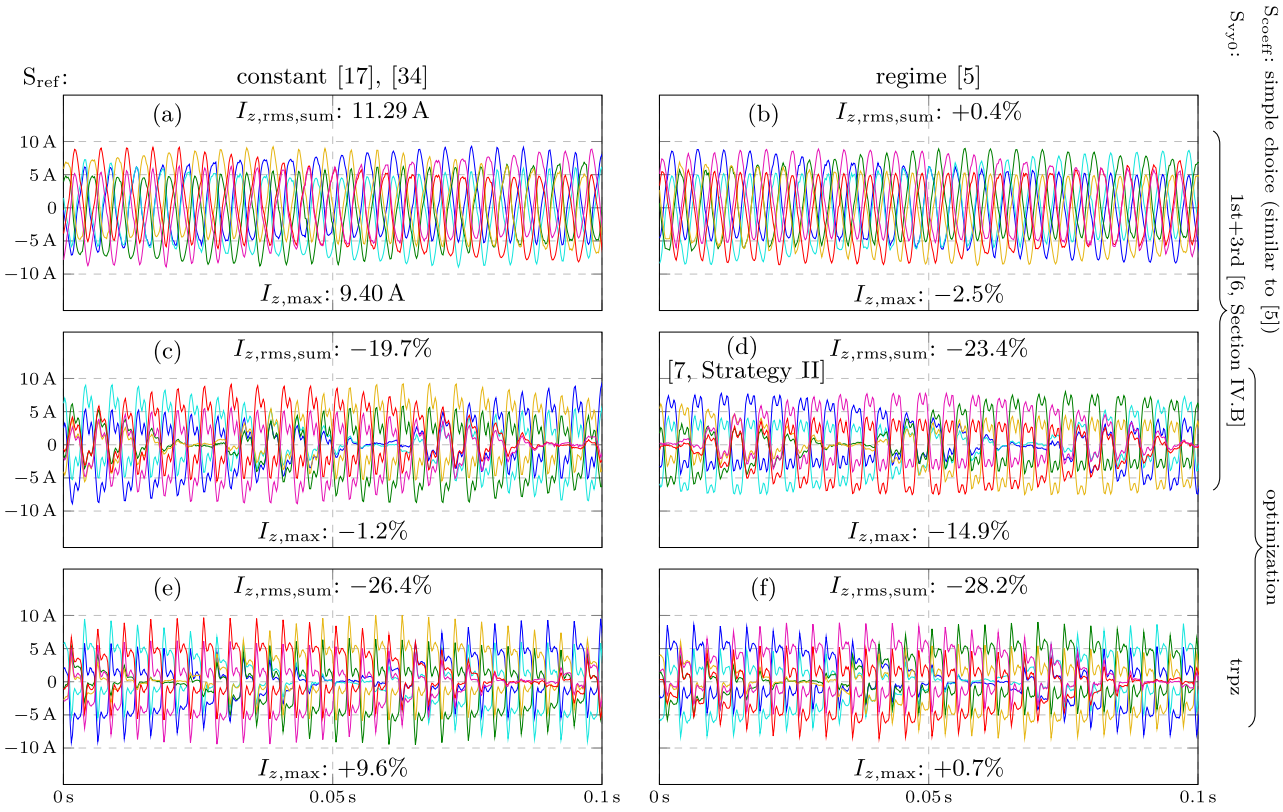

Fig. 9. Measurement results of the six arm currents during the stationary operation at $\omega_\mathrm{m} = 2\pi \cdot 5\,\mathrm{Hz}$ (4% p.u.) and $i_\mathrm{q} = -3.7\,\mathrm{A}$.

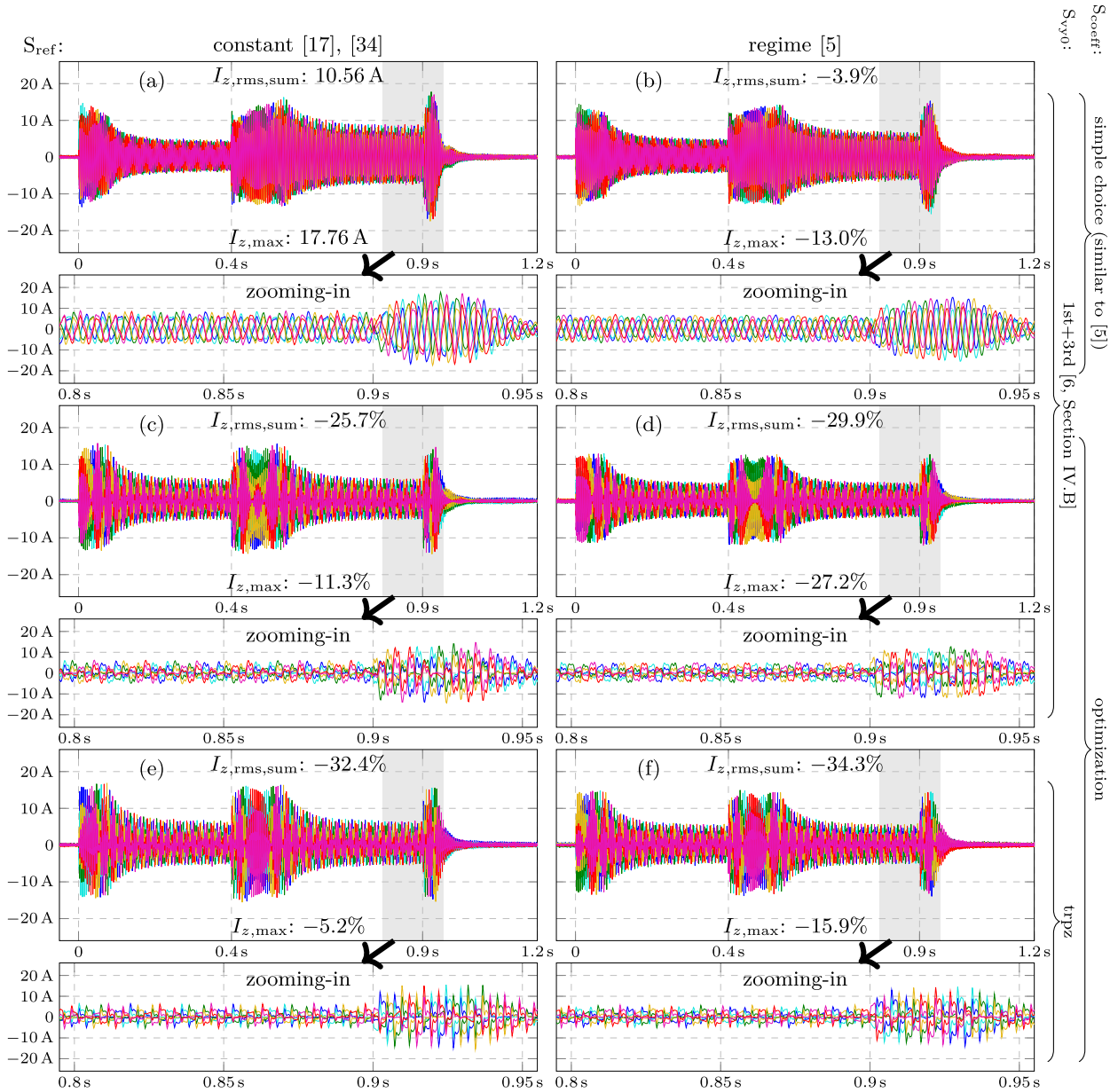

Fig. 10. Measurement results of the six arm currents during the test process shown in Fig. 6.

load torque in both rotating directions. On the whole, although a current control error exists and the observer output cannot track the speed varying load torque exactly during the speed transient, the speed control is accomplished without any overshoot. The reason of the current control error is suspected to be the nonideal decoupling between the d- and q-axis current, while the transient of the observer is expected, since the conditions for the desired dynamic (33) include a constant load torque.

The measurement results of the six arm currents and equivalent cell capacitor voltages w.r.t. the proposed energy control with different options are shown in Figs. 10 and 11 with zooming-in for a detailed description of the trajectories, respectively.

The subfigures have the same organization as in Figs. 8 and 9. The results are analyzed as follows.

1) First of all, the results verify the stability of the energy control system in Fig. 4 under the tested stator electrical frequency profile in Fig. 6(b), since the measured trajectories in Figs. 10 and 11 do not increase or decrease permanently. This is not included by the theoretical conclusion in Section IV-E since the theoretical analysis assumes a constant stator electrical frequency.
2) The two options for the energy reference are compared by means of (a), (c), (e) and (b), (d), (f), respectively. Regarding the defined indexes, the regime as reference [5] shows better transient performance than the constant reference [17], [34].
3) The two options for the energy controller and compensation of ripples at low frequency are compared by means of (a), (b) and (c), (d), respectively. In cooperation with the

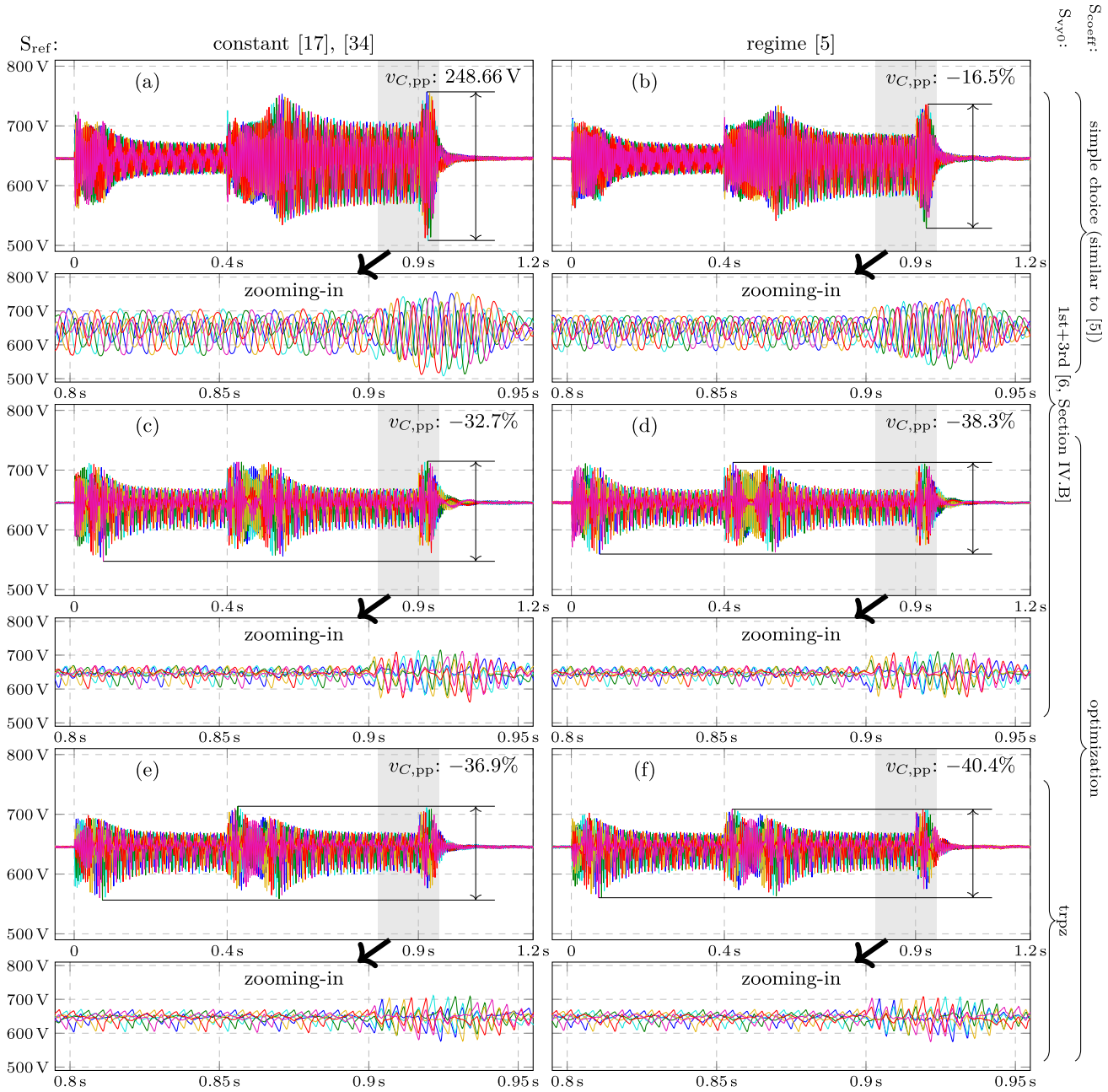

Fig. 11. Measurement results of the six equivalent cell capacitor voltages during the test process shown in Fig. 6.

same common-mode voltage $v_{y0}^{1\mathrm{st}+3\,\mathrm{rd}}$ [6, Sec. IV-B], the optimization reduces not only the current indexes $I_{z,\max}$ and $I_{z,\mathrm{rms,sum}}$, but also the peak-to-peak value $v_{C,\mathrm{pp}}$ of the equivalent cell capacitor voltage ripples, compared with the simple choice (similar to [5]).

4) The two options for the common-mode voltages are compared by means of (c), (d) and (e), (f), respectively. In cooperation with the optimization, the approximated trapezoidal waveform v_{y0}^{trpz} leads to smaller arm current RMS $I_{z,\mathrm{rms,sum}}$ and smaller peak-to-peak value $v_{C,\mathrm{pp}}$ of the six equivalent cell capacitor voltages, compared to $v_{y0}^{1\mathrm{st}+3\,\mathrm{rd}}$ [6, Sec. IV-B]. However, the peak arm current $I_{z,\max}$ is larger than the case with $v_{y0}^{1\mathrm{st}+3\,\mathrm{rd}}$. The reason is suspected to be the challenging current control task, since the approximated trapezoidal waveform v_{y0}^{trpz} enables current harmonics of higher order, leading to requirement of improved current control than the current test bench setting.

4) Summary: To sum up, the experiments verify the theoretical conclusion in Section IV-E, i.e., the MMC energies track the designed stationary regime, or it approaches a stationary operation with ripples around the constant reference $\boldsymbol{E}$. The stability of the energy control system at varying stator electrical frequency is also verified experimentally, which is not included

in the theoretical conclusion. Furthermore, the experiments also offer a dedicated comparison between the options in the energy control system in Fig. 4 by means of the defined performance indexes. The comparison between the constant reference $\boldsymbol{E}$ [17], [34] and the regime as energy reference [5] is provided for the first time. Although the constant reference $\boldsymbol{E}$ increases the performance indexes slightly, it is still a noteworthy option, since it spares the costly regime calculation. Compared with the simple choice (similar to [5]), the optimization—especially in cooperation with the approximated trapezoidal common-mode voltage v_{y0}^{trpz}—reduces the peak-to-peak cell capacitor voltage ripples and the arm current RMS substantially. This includes the optimized regime/operation generated by the optimization in cooperation with v_{y0}^{trpz} as an improvement of [7, Strategy II] in the sense of smaller arm current RMS and cell capacitor voltage fluctuation. Compared with $v_{y0}^{1\text{st}+3\,\text{rd}}$ [6, Sec. IV-B], the approximated trapezoidal common-mode voltage v_{y0}^{trpz} reduces the arm current RMS and cell capacitor voltage fluctuation at a cost of higher peak arm current due to more challenging current control.

VI. Conclusion

This work extends the results in [10] for MMC dc-operation (0 Hz) to lf-mode for drive applications. Thus, this work covers the results for dc-operation (0 Hz) in [10] as a specific case, and inherits all improvements of [10] w.r.t. model based controller design, compared to [5], [9], [19], [23], [24], [25], [26], [27], and [28] (as mentioned before Section I-A). Using the general averaging (4) which extends the averaging method for dc-operation (0 Hz) in [10] to the almost-periodic cases in lf-mode, the proposed control system for the MMC energies in lf-mode is derived. As an extension from the stability analysis for dc-operation in [10], Theorem 1 in Appendix provides a rigorous global stability of the energy control system for lf-mode in which the instantaneous MMC energy either converges globally to a neighborhood of the constant reference $\boldsymbol{E}$ (same idea for reference in [17], [34]) or tracks the calculated stationary operating regime (same idea for reference in [5]), unlike [7], [27], [30] which only provide a region of attraction in an uncertain small neighborhood of a stationary operating regime/point. The validity of a constant reference for the instantaneous MMC energies in lf-mode is confirmed by dedicated theoretical analysis for the first time. Besides, an optimized variant in cooperation with all harmonics in the common-mode voltage for the energy control and compensation of ripples at low frequency is derived by quadratic programming.

The experiments verify the stability of the energy control system in the sense of the theoretical conclusions and also at varying stator electrical frequency which is not included by the theoretical conclusions. The options in the energy control system are compared by experiments with defined performance indexes, in which the comparison between the constant reference $\boldsymbol{E}$ [17], [34] and the regime as energy reference [5] is provided for the first time. Although the constant reference $\boldsymbol{E}$ increases the performance indexes slightly, it is still a noteworthy option, since it spares the costly regime calculation. Compared with the simple choice (similar to [5]), the optimization—especially in cooperation with the approximated trapezoidal common-mode voltage v_{y0}^{trpz}—reduces the peak-to-peak cell capacitor voltage ripples and the arm current RMS substantially. This includes the optimized stationary regime/operation generated by the optimization in cooperation with v_{y0}^{trpz} as an improvement of [7, Strategy II] in the sense of smaller arm current RMS and cell capacitor voltage fluctuation. Compared with $v_{y0}^{1\text{st}+3\,\text{rd}}$ [6, Sec. IV-B], the approximated trapezoidal common-mode voltage v_{y0}^{trpz} decreases the arm current RMS and cell capacitor voltage fluctuation at a cost of higher peak arm current due to more challenging current control.

The general averaging method presented in this work is compatible with almost periodic systems which are affected by several frequencies. Therefore, it is expected to be applied to the controller design of other topologies like modular multilevel matrix converter (M3C).

Appendix

Definition 1: A continuous, bounded function $\boldsymbol{f}:[0,\infty)\times\mathbb{D}\to\mathbb{R}^n$ is said to have a general average $\overline{\boldsymbol{f}}(\boldsymbol{x})$ if the limit given in (4) exist and

$$\left\|\frac{1}{T}\int_t^{t+T}\boldsymbol{f}\left(\tau,\boldsymbol{x}\right)\mathrm{d}\tau-\overline{\boldsymbol{f}}\left(\boldsymbol{x}\right)\right\|\leq c\cdot f_{\text{cvg}}(T) \tag{35}$$

for some $c>0$, $\forall(t,\boldsymbol{x})\in[0,\infty)\times\mathbb{D}_0$, and $\forall\mathbb{D}_0\subset\mathbb{D}$, where $\boldsymbol{x}$ is regarded to be independent of t while considering the integral in (4) and (35). The function $f_{\text{cvg}}(T)$ is called the convergence function which is strictly decreasing, continuous, and bounded such that $\lim_{T\to\infty}f_{\text{cvg}}(T)=0$. □

Theorem 1: Suppose an n-dimensional function $\boldsymbol{f}(t,\boldsymbol{x},\varepsilon)$ satisfies the following conditions.

C1: The function $\boldsymbol{f}(t,\boldsymbol{x},\varepsilon)$ and its partial derivatives w.r.t. $(\boldsymbol{x},\varepsilon)$ up to the second order are continuous and bounded for $(t,\boldsymbol{x},\varepsilon)\in[0,\infty)\times\mathbb{D}_1\times[0,\varepsilon_1]$, for every compact set $\mathbb{D}_1\subset\mathbb{D}_2$, where $\varepsilon_1>0$ and $\mathbb{D}_2\subset\mathbb{R}^n$ is a domain.

C2 : The function $\boldsymbol{f}(t,\boldsymbol{x},0)$ has the general average $\overline{\boldsymbol{f}}(\boldsymbol{x})$ on $(t,\boldsymbol{x})\in[0,\infty)\times\mathbb{D}_2$ with the convergence function $f_{\text{cvg}}(T)$, in the sense of Definition 1.

C3: The Jacobian $\frac{\partial}{\partial\boldsymbol{x}}(\boldsymbol{f}(t,\boldsymbol{x},0)-\overline{\boldsymbol{f}}(\boldsymbol{x}))$ has zero general average with the same convergence function $f_{\text{cvg}}(T)$ as $\boldsymbol{f}(t,\boldsymbol{x},0)$.

C4: The initial values of the solution $\boldsymbol{x}(t)$ of the original system (5) and the solution $\overline{\boldsymbol{x}}(t)$ of the average system (6) satisfy $\overline{\boldsymbol{x}}(0)=\boldsymbol{x}(0)$.

C5: The origin $\overline{\boldsymbol{x}}=\boldsymbol{0}\in\mathbb{D}_2$ is an exponentially stable equilibrium point of the average system (6) and $\overline{\boldsymbol{x}}(0)\in\mathbb{D}_3$, where $\mathbb{D}_3\subset\mathbb{D}_2$ is a compact subset of its region of attraction.

Then, there exist $\varepsilon_2>0$ and a strictly increasing function $f_{\mathcal{K}}(\varepsilon)\geq 0$ with $f_{\mathcal{K}}(0)=0$, such that for all $0<\varepsilon<\varepsilon_2$, $\boldsymbol{x}(t)$ is defined and

$$\|\boldsymbol{x}(t)-\overline{\boldsymbol{x}}(t)\|\leq c_2 f_{\mathcal{K}}\left(\varepsilon\right) \tag{36}$$

for some $c_2>0$ and $\forall t\in[0,\infty)$, and the origin of the original system (5) is exponentially stable if the following additional condition is satisfied.

C6 : The origin is an equilibrium point of the original system (5), i.e., (7) for $\forall(t,\varepsilon) \in [0,\infty) \times [0,\varepsilon_1]$. □

ACKNOWLEDGMENT

The testbench for the experiments is provided by Chair of Power Electronics, TU Dresden, Germany.

REFERENCES

[1] R. Marquardt, "Modular multilevel converter: An universal concept for HVDC-networks and extended DC-bus-applications," in *Proc. Int. Power Electron. Conf. - ECCE ASIA*, 2010, pp. 502–507.

[2] S. Wenig, F. Rojas, K. Schönleber, M. Suriyah, and T. Leibfried, "Simulation framework for DC grid control and ACDC interaction studies based on modular multilevel converters," *IEEE Trans. Power Del.*, vol. 31, no. 2, pp. 780–788, Apr. 2016.

[3] G. Bergna-Diaz, J. Freytes, X. Guillaud, S. D. Arco, and J. A. Suul, "Analysis of MMC dynamics in DQZ coordinates for vertical and horizontal energy balancing control," in *Proc. IEEE IECON - 44th Annu. Conf. Ind. Electron. Soc.*, 2018, pp. 5999–6006.

[4] S. Allebrod, R. Hamerski, and R. Marquardt, "New transformerless, scalable modular multilevel converters for HVDC-transmission," in *Proc. IEEE Power Electron. Specialists Conf.*, 2008, pp. 174–179.

[5] J. Kolb, F. Kammerer, M. Gommeringer, and M. Braun, "Cascaded control system of the modular multilevel converter for feeding variable-speed drives," *IEEE Trans. Power Electron.*, vol. 30, no. 1, pp. 349–357, Jan. 2015.

[6] M. Hagiwara, I. Hasegawa, and H. Akagi, "Start-up and low-speed operation of an electric motor driven by a modular multilevel cascade inverter," *IEEE Trans. Ind. Appl.*, vol. 49, no. 4, pp. 1556–1565, Jul./Aug. 2013.

[7] S. Debnath, J. Qin, and M. Saeedifard, "Control and stability analysis of modular multilevel converter under low-frequency operation," *IEEE Trans. Ind. Electron.*, vol. 62, no. 9, pp. 5329–5339, Sep. 2015.

[8] A. Antonopoulos, K. Ilves, L. Ängquist, and H.-P. Nee, "On interaction between internal converter dynamics and current control of high-performance high-power ac motor drives with modular multilevel converters," in *Proc. IEEE Energy Convers. Congr. Expo.*, 2010, pp. 4293–4298.

[9] M. Espinoza, R. Cárdenas, M. Díaz, A. Mora, and D. Soto, "Modelling and control of the modular multilevel converter in back to back configuration for high power induction machine drives," in *Proc. IEEE IECON - 42nd Annu. Conf. Ind. Electron. Soc.*, 2016, pp. 5046–5051.

[10] Q. Gui, H. Fehr, and A. Gensior, "Stability assessment and optimization of MMC energy balancing for drive applications at standstill using an averaging approach," in *Proc. 24th Eur. Conf. Power Electron. Appl.*, 2022, pp. 1–10.

[11] M. A. Perez, S. Ceballos, G. Konstantinou, J. Pou, and R. P. Aguilera, "Modular multilevel converters: Recent achievements and challenges," *IEEE Open J. Ind. Electron. Soc.*, vol. 2, pp. 224–239, 2021.

[12] S. Fuchs, S. Beck, and J. Biela, "Analysis and reduction of the output voltage error of PWM for modular multilevel converters," *IEEE Trans. Ind. Electron.*, vol. 66, no. 3, pp. 2291–2301, Mar. 2019.

[13] S. Rohner, S. Bernet, M. Hiller, and R. Sommer, "Modulation, losses, and semiconductor requirements of modular multilevel converters," *IEEE Trans. Ind. Electron.*, vol. 57, no. 8, pp. 2633–2642, Aug. 2010.

[14] H. Fehr, A. Gensior, and S. Bernet, "Experimental evaluation of PWM-methods for modular multilevel converters," in *Proc. 18th Eur. Conf. Power Electron. Appl.*, 2016, pp. 1–10.

[15] M. Hagiwara and H. Akagi, "Control and experiment of pulsewidth-modulated modular multilevel converters," *IEEE Trans. Power Electron.*, vol. 24, no. 7, pp. 1737–1746, Jul. 2009.

[16] D. Karwatzki, L. Baruschka, M. Dokus, J. Kucka, and A. Mertens, "Branch energy balancing with a generalised control concept for modular multilevel topologies — using the example of the modular multilevel converter," in *Proc. 18th Eur. Conf. Power Electron. Appl.*, 2016, pp. 1–10.

[17] R. Lizana, M. A. Perez, S. Bernet, J. R. Espinoza, and J. Rodriguez, "Control of arm capacitor voltages in modular multilevel converters," *IEEE Trans. Power Electron.*, vol. 31, no. 2, pp. 1774–1784, Feb. 2016.

[18] H. Fehr and A. Gensior, "Eigenvalue optimization of the energy-balancing feedback for modular multilevel converters," *IEEE Trans. Power Electron.*, vol. 34, no. 11, pp. 11482–11495, Nov. 2019.

[19] A. Gensior and H. Fehr, "Modeling and energy balancing control of modular multilevel converters using perturbation theory for quasi-periodic systems," *IEEE Trans. Power Electron.*, vol. 36, no. 2, pp. 2201–2217, Feb. 2021.

[20] H. Bärnklau, A. Gensior, and J. Rudolph, "A model-based control scheme for modular multilevel converters," *IEEE Trans. Ind. Electron.*, vol. 60, no. 12, pp. 5359–5375, Dec. 2013.

[21] H. Fehr and A. Gensior, "Model-based circulating current references for MMC cell voltage ripple reduction and loss-equivalent arm current assessment," in *Proc. 21st Eur. Conf. Power Electron. Appl.*, 2019, pp. P.1–P.9.

[22] S. Rohner, J. Weber, and S. Bernet, "Continuous model of modular multilevel converter with experimental verification," in *Proc. IEEE Energy Convers. Congr. Expo.*, 2011, pp. 4021–4028.

[23] A. E. Leon and S. J. Amodeo, "Energy balancing improvement of modular multilevel converters under unbalanced grid conditions," *IEEE Trans. Power Electron.*, vol. 32, no. 8, pp. 6628–6637, Aug. 2017.

[24] A. Christe and D. Dujic, "Modular multilevel converter control methods performance benchmark for medium voltage applications," *IEEE Trans. Power Electron.*, vol. 34, no. 5, pp. 4967–4980, May 2019.

[25] Ö. C. Sakinci and J. Beerten, "Generalized dynamic phasor modeling of the MMC for small-signal stability analysis," *IEEE Trans. Power Del.*, vol. 34, no. 3, pp. 991–1000, Jun. 2019.

[26] J. Rupasinghe, S. Filizadeh, and L. Wang, "A dynamic phasor model of an MMC with extended frequency range for EMT simulations," *IEEE Trans. Emerg. Sel. Topics Power Electron.*, vol. 7, no. 1, pp. 30–40, Mar. 2019.

[27] Y. Ma, H. Lin, Z. Wang, and Z. Ze, "Stability analysis of modular multilevel converter based on harmonic state-space theory," *IET Power Electron.*, vol. 12, no. 15, pp. 3987–3997, 2019. [Online]. Available: https://ietresearch.onlinelibrary.wiley.com/doi/abs/10.1049/iet-pel.2019.0613

[28] J. Lyu, X. Zhang, X. Cai, and M. Molinas, "Harmonic state-space based small-signal impedance modeling of a modular multilevel converter with consideration of internal harmonic dynamics," *IEEE Trans. Power Electron.*, vol. 34, no. 3, pp. 2134–2148, Mar. 2019.

[29] H. K. Khalil, *Nonlinear Systems*, 3rd ed., Englewood Cliffs, NJ, USA: Prentice Hall, 2002.

[30] L. Harnefors, A. Antonopoulos, S. Norrga, L. Angquist, and H. Nee, "Dynamic analysis of modular multilevel converters," *IEEE Trans. Ind. Electron.*, vol. 60, no. 7, pp. 2526–2537, Jul. 2013.

[31] A. J. Korn, M. Winkelnkemper, and P. Steimer, "Low output frequency operation of the modular multi-level converter," in *Proc. IEEE Energy Convers. Congr. Expo.*, 2010, pp. 3993–3997.

[32] Y. Okazaki, H. Matsui, M. M. Muhoro, M. Hagiwara, and H. Akagi, "Capacitor-voltage balancing for a modular multilevel DSCC inverter driving a medium-voltage synchronous motor," *IEEE Trans. Ind. Appl.*, vol. 52, no. 5, pp. 4074–4083, Sep./Oct. 2016.

[33] A. M. Fink, *Almost Periodic Differential Equations*. Berlin, Germany: Springer, Jan. 1, 1974.

[34] J. Jung, H. Lee, and S. Sul, "Control strategy for improved dynamic performance of variable-speed drives with modular multilevel converter," *IEEE Trans. Emerg. Sel. Topics Power Electron.*, vol. 3, no. 2, pp. 371–380, Jun. 2015.

[35] Q. Gui, H. Fehr, and A. Gensior, "Optimized stationary operating regime and common-mode voltage design for modular multilevel converters in drive applications at high frequency," in *Proc. 25th Eur. Conf. Power Electron. Appl.*, 2023, pp. 1–10.

[36] A. Antonopoulos, L. Ängquist, S. Norrga, K. Ilves, L. Harnefors, and H. Nee, "Modular multilevel converter AC motor drives with constant torque from zero to nominal speed," *IEEE Trans. Ind. Appl.*, vol. 50, no. 3, pp. 1982–1993, May/Jun. 2014.

[37] Y. Okazaki, M. Hagiwara, and H. Akagi, "A speed-sensorless start-up method of an induction motor driven by a modular multilevel cascade inverter (MMCI-DSCC)," *IEEE Trans. Ind. Appl.*, vol. 50, no. 4, pp. 2671–2680, Jul./Aug. 2014.

[38] M. Espinoza-B et al., "An integrated converter and machine control system for MMC-based high-power drives," *IEEE Trans. Ind. Electron.*, vol. 66, no. 3, pp. 2343–2354, Mar. 2019.

[39] M. Espinoza, R. Cárdenas, M. Díaz, and J. C. Clare, "An enhanced *dq*-based vector control system for modular multilevel converters feeding variable-speed drives," *IEEE Trans. Ind. Electron.*, vol. 64, no. 4, pp. 2620–2630, Apr. 2017.

[40] M. Espinoza, M. Díaz, E. Espina, C. M. Hackl, and R. Cardenas, "Control strategies for modular multilevel converters driving cage machines," in *Proc. IEEE Southern Power Electron. Conf.*, 2017, pp. 1–6.

[41] B. M. Espinoza, A. Mora, M. Diaz, and R. Cárdenas, "Balancing energy and low frequency operation of the modular multilevel converter in back to back configuration," in *Proc. Tenth Int. Conf. Ecological Veh. Renewable Energies*, 2015, pp. 1–9.

[42] B. Li et al., "An improved circulating current injection method for modular multilevel converters in variable-speed drives," *IEEE Trans. Ind. Electron.*, vol. 63, no. 11, pp. 7215–7225, Nov. 2016.

[43] M. Soares and E. H. Watanabe, "MMC applied to pumped hydro storage using a differentiable approximation of a square wave as common-mode voltage during low-frequency operation," in *Proc. IEEE 21st Workshop Control Model. Power Electron.*, 2020, pp. 1–8.

[44] A. Antonopoulos, L. Ängquist, S. Norrga, K. Ilves, and H. Nee, "Modular multilevel converter AC motor drives with constant torque form zero to nominal speed," in *Proc. IEEE Energy Convers. Congr. Expo.*, 2012, pp. 739–746.

[45] D. Graham and R. C. Lathrop, "The synthesis of "optimum" transient response: Criteria and standard forms," *Trans. Amer. Inst. Elect. Engineers, Part II: Appl. Ind.*, vol. 72, no. 5, pp. 273–288, Nov. 1953.

[46] R. Dierks, J. Kucka, and A. Mertens, "Using both the circulating currents and the common-mode voltage for the branch energy control of modular multilevel converters," in *Proc. 22nd Eur. Conf. Power Electron. Appl.*, 2020, pp. P.1–P.10.

[47] Q. Gui, J. L. Gnärig, H. Fehr, and A. Gensior, "Energy-balancing of a modular multilevel converter using an online trajectory planning algorithm," in *Proc. 22nd Eur. Conf. Power Electron. Appl.*, 2020, pp. P.1–P.10.

[48] Q. Gui, H. Fehr, and A. Gensior, "Energy-balancing of a modular multilevel converter with pulsed DC load using an online trajectory planning algorithm," in *Proc. 23rd Eur. Conf. Power Electron. Appl.*, 2021, pp. P.1–P.10.

[49] S. Debnath and M. Saeedifard, "Simulation-based gradient-descent optimization of modular multilevel converter controller parameters," *IEEE Trans. Ind. Electron.*, vol. 63, no. 1, pp. 102–112, Jan. 2016.

[50] E. Delaleau and A. M. Stankovic, "Flatness-based hierarchical control of the PM synchronous motor," in *Proc. Amer. Control Conf.*, 2004, pp. 65–70.